Yttrium complexation and hydration in chloride-rich hydrothermal fluids: A combined ab initio molecular dynamics and in situ X-ray absorption spectroscopy study

Qiushi Guan, Yuan Mei, Barbara Etschmann, Denis Testemale, Marion Louvel, Joël Brugger

Yttrium complexation and hydration in chloride-rich hydrothermal fluids: a combined *ab initio* molecular dynamics and *in situ* X-ray absorption spectroscopy study

Qiushi Guan[1,2], Yuan Mei[2*], Barbara Etschmann[1], Denis Testemale[3], Marion Louvel[4], Joël Brugger[1*]

1. School of Earth, Atmosphere and the Environment, Monash University, Clayton, VIC 3800, Australia
2. CSIRO Mineral Resources, Kensington WA 6152, Australia
3. CNRS, Université Grenoble Alpes, Institut NEEL, F-38000 Grenoble, France
4. Institute for Mineralogy, WWU Muenster, D-48149 Germany

*Corresponding author: Yuan Mei (Yuan.Mei@csiro.au); Joël Brugger (joel.brugger@monash.edu)

Abstract

Accurate knowledge of rare earth elements (REE) speciation in high pressure – high temperature fluids is required to model REE transport and precipitation in subduction zones and magmatic-hydrothermal environments, and the formation of rare metal deposits. Recent experiments (lanthanum, ytterbium, erbium) have demonstrated that REE chloride complexes are the main REE form in many hydrothermal fluids (Migdisov, et al., 2016). However, the speciation of yttrium

(Y(III)), a cation with an ionic radius similar to that of Ho(III), remains poorly constrained in chloride-rich hydrothermal solutions.

We used *ab initio* molecular dynamics (MD) simulations to calculate the nature of Y(III)-Cl complexes and the thermodynamic properties of these species at temperatures up to 500 ºC and pressures of 800 bar and 1000 bar. The MD results were complemented by *in-situ* X-ray absorption spectroscopy (XAS) measurements. Our results indicate that at temperature below 200 ºC, chloro-complexes do not form readily, even in highly concentrated brines. At ambient condition, the Y(III) aqua ion binds to eight water molecules in a square antiprism geometry, which is consistent with previous *ab initio* studies (Ikeda, et al., 2005). The thermodynamic integration method was employed to calculate the formation constants (logβ) of Y(III)-Cl^- complexes in two simulation boxes containing different Y:Cl ratios; we obtained very consistent results of the standard logβ of same complexes from the two independent calculations, which confirms that the thermodynamic integration method is reliable and not significantly affected by technical limitations in box size, box composition, or simulation times.

Based on the derived formation constants, we fit Modified Ryzhenko–Bryzgalin (MRB) equation of state parameters, which enable extrapolation of the formation constants at elevated temperature and pressure. The results are consistent with the XAS data, and show that the stability of Y(III)-Cl complexes increases with increasing temperature, Y(III) forming high order Cl^- complexes (up to YCl_4^-) in high

salinity solutions at high temperature and pH = 3. We also compare the extrapolated logβ with the available data for other REE at 150 ˚C, 200 ˚C and 250 ˚C. At 200 ˚C, yttrium behaves more like a heavy REE, but from 200 ˚C to 250 ˚C, the logβ of Y(III)-Cl complexes increases dramatically and behave more like the light REE. The difference of Cl^- dominant species between Ho(III) ($HoCl^{2+}$) and Y(III) (YCl_2^+) may account for the formation of anomalous Y/Ho ratios in some hydrothermal environments.

Keywords: Yttrium; *ab initio* molecular dynamics; XAS; yttrium chloride aqueous speciation; thermodynamics; rare earth elements.

1. Introduction

Demand for rare earth elements (REE: La to Lu) plus Y has increased in the past decades due to their use in fast-growing industrial applications (e.g., energy, mobility and special alloys; Krishnamurthy, 2016). Combined with strategic issues related to current concentration of REE production within China, this has led to world-wide efforts to secure new geological sources of REE (Weng et al., 2015; Ram et al. 2018). The world's largest REE deposit formed by a combination of magmatic and hydrothermal processes (Bayan Obo, China; Ling et al., 2013). REE are mobile in many hydrothermal systems (e.g., Iron Oxide Copper Gold deposits and their alteration halos; (Kontonikas-Charos et al., 2018; Xing et al., 2019), and since REE behave coherently through geochemical processes, they can be used as tracers for fluid-rock interaction (e.g., Bau and Dulski, 1995; Brugger et al., 2008). Over the past decade, a number of experimental studies have dramatically improved our understanding of REE speciation in natural water at elevated temperature, e.g. *in situ* measurements at high temperature-pressure for Yb (Louvel et al. 2015) and Eu (Liu et al. 2017); solubility experiments of REE+Y-fluoride (Loges et al. 2013; Migdisov 2009); *in situ* spectrophotometric studies of REE chloride and sulfate complexes (Migdisov and Williams-Jones, 2008; Migdisov et al. 2008). As reviewed by Migdisov et al. (2016), the nature of REE complexes (e.g., chloride versus fluoride or hydroxide complexes) affects mineral solubility, and is controlled by temperature, pressure and solution composition.

A molecular-level understanding of the coordination geometry and hydration of the complexes is key to reliable extrapolations of thermodynamic properties that can be also used to model metal mobility beyond the conditions covered by experiments (Brugger et al., 2016). Chloride is the most common ligand in many geo-fluids, and despite the fact that REE fluoride complexes are much stronger than chloride complexes (Haas et al., 1995; Wood, 1990), chloride complexes are considered as the main transporting ligands in many hydrothermal fluids, especially at high temperature, since the stability of chloride complexes increases with increasing temperature relative to fluoride complexes, and the activity of the fluoride ion is limited by the strong association of hydrofluoric acid at elevated temperature and the low solubility of fluorine-containing phases such are fluorite, apatite, and biotite (Gammons et al., 1996; Migdisov et al., 2009; Xing et al. 2019).

The similar chemical properties of REE *sensu stricto* (lanthanides) are a result of their valence electrons in *4f*-obitals; these *f*-electrons are buried deep within the atom and shielded by *4d* and *5p* electrons and do not take part in bonding. Yttrium is often grouped with REE because its ionic radius (0.900 Å for Y^{3+}) is close to that of the heavy REE (Ho^{3+} at 0.901 Å; Shannon, 1976). However, due to its lack of *f*-electrons ([Kr] $4d^1\ 5s^2$), Y(III) shows significant differences in behavior compared to REE *sensu stricto*. For example, Loges (2013) showed that at temperatures below 250 ºC, the dominant Y(III) fluoride complex is YF^{2+}, compared to $REEF_2^+$ (HoF_2^+). These differences can result in contrasting mobility of Y and REE in hydrothermal systems

98 (Williams-Jones, 2009), leading to the concept of 'yttrium anomaly' (Bau and Dulski,
99 1995).

100 Several experiments have been conducted on the hydration of Y(III) at low
101 temperature (Table 1). At room temperature, the Y(III) aqua ion is generally
102 recognized to have a coordination of 8 and a square antiprism structure (references in
103 Table 1). The early *in-situ* XAS study of Ragnarsdottir et al. (1998) provides the only
104 experimental data on Y(III) hydration under hydrothermal conditions. Ragnarsdottir et
105 al. (1998) obtained a higher than expected Y(III) hydration number at room
106 temperature (9.1 – 10.3), and showed a small decrease in hydration number to 8 at
107 temperature of 250 ºC, with no further dehydration observed upon heating to 340 ºC.

108 There are only a few studies about Y(III) chloride complexing, and again
109 Ragnarsdottir et al. (1998) is the only experimental study extending to hydrothermal
110 conditions (Table 1). Conclusions regarding the extent of Y-Cl complexation differ.
111 On one hand, Allen et al. (2000)'s EXAFS study found no evidence for Cl^- bonded
112 with Y(III) at ambient temperature, even in brines containing up to 14 m Cl^-.
113 Ragnarsdottir et al. (1998) similarly found no evidence of Y-Cl complexing in a 0.1 m
114 YCl_3 solution to 340 ºC, and in a 0.1 m YCl_3 + 0.23 m HCl + 2 m NaCl solution to
115 250 ºC (Cl_{tot} = 2.53 m). On the other hand, Luo and Byrne (2001) report a stability
116 constant of 0.65 ± 0.05 for the formation of YCl^{2+} (reaction $Y^{3+} + Cl^- = YCl^{2+}$) at
117 25 ºC and zero ionic strength, and concluded that Y^{3+} formed weak complexes with
118 Cl^-. Combining neutron scattering and EXAFS spectroscopy, Bowron and

Diaz-Moreno (2007) also support the formation of Y-Cl complexes in 1 m YCl_3 solution at room temperature, with a hydration number of 7.4 ± 0.5 in the distance between 2.1 Å and 3.3 Å, and 0.8 ± 0.2 Cl^- between 2.5 Å and 3.5 Å, from the radial distribution functions of Y-O and Y-Cl. Rudolph and Irmer (2015) concluded in a recent Raman study that Y(III) and Cl^- can form weak chloro-complexes at room temperature in YCl_3+HCl solutions (2.03 M YCl_3 in 1.0 M and 4 M HCl). They propose that Y exists in 8-fold coordination as $[Y(H_2O)_{8-n}Cl_n]^{+3-n}$ in these solutions, with chloride numbers $n \leqslant 2$. Stefanski and Jahn (2019) studied Y(III) speciation in chloride- and fluoride-rich brines under subduction conditions (800 ˚C, 13/45 kbar) with *ab initio* molecular dynamics, and concluded that chloride complexes $[Y(H_2O)_{2-7}Cl_{1-5}]^{+3-n(Cl)}$ are important species of Y mass transfer in subduction zones.

Table 1. Structure of aqueous Y(III) in literature

In this study, we combined *ab initio* molecular dynamics (MD) simulations and *in situ* XAS measurements to quantify the nature, geometry, and stability of Y(III) complexes in chlorine-rich fluids from room temperature to 500 ºC, 1000 bar. In particular, the formation constants of Y(III)-Cl complexes were calculated from *ab initio* MD using the thermodynamic integration method. Our previous studies have demonstrated that the combination of *ab initio* computational chemistry and *in situ* spectroscopic experiments is a powerful approach to determining element speciation and geometry in hydrothermal fluids (Mei et al., 2015a,b, 2016; Brugger et al., 2016; Etschmann et al., 2018, 2019), providing accurate speciation data that can be used to

provide extrapolations to conditions beyond experimental scope.

2. Method

2.1 Ab initio molecular dynamics

The *ab initio* MD simulations were conducted with Car-Parrinello Molecular Dynamics (CPMD, version 3.1.17, Car and Parrinello, 1985). In CPMD, the electrons were treated as plane wave basis sets using density functional theory. The interactions between valence electrons were depicted by BLYP exchange correlation functional (Becke, 1988; Lee et al., 1988), which produces a good description of the structural properties of water including O–O interaction, angular distributions, coordination numbers, H-bond statistics, and radial distribution functions when compared with experiments (Gillan et al., 2016; Lin et al., 2012). However, most generalized gradient approximation functionals, including BLYP, tend to overestimate the ordering of the structure of liquid water at ambient condition (e.g., Sprik, et al. 1996, Mei et al., 2018). Bankura et al. (2014) showed that BLYP best reproduces the properties of water at ambient conditions when using an elevated temperature for the simulations, and it could be argued that there is a temperature offset of approximately 55˚C between the computed data and experiment in terms of solvent properties. Despite these limitations, many previous studies obtained accurate results of aqueous metal-ligand complexations at both room and high temperature using the BLYP functional (e.g. Mei et al., 2015b; Stefanski and Jahn, 2019). A timestep of 3 a.u. (0.073 fs) and fictitious mass of 400 a.u. to all atoms were employed in the simulation.

We used the NVT ensemble to conduct the simulations. The density of the solution was chosen according to the equation of state of NaCl solution at similar chloride concentration at targeted T and P (Driesner, 2007; Driesner and Heinrich, 2007). The temperature was fixed with Nosé-Hoover chain thermostat for ions and electrons. Periodic boundary condition was applied to eliminate surface effects.

In total, 15 *ab initio* MD simulations were conducted over a range of temperatures (25-500 ºC), pressures (1, 800 and 1000 bar), and compositions (simulation boxes containing 1 yttrium(III) ion, 3 to 5 chloride ion, and 55 or 110 H_2O molecules) relevant for a wide range of hydrothermal systems; the simulation details are listed in Table 2. All the MD simulations were conducted for 16-30 picoseconds (ps) in order to achieve good statistics. As discussed in our previous study (Mei et al., 2013a), the size of the simulation boxes and times in this study can provide solid results within manageable computation resources. The time-averaged stoichiometric and geometric information was obtained with VMD (Humphrey et al., 1996). The coordination numbers were retrieved from radial distribution functions (RDF), and their errors were estimated from the change of RDF integral at the distance range of 2.75 Å - 3.25 Å for Y-O, and 2.9 Å – 3.2 Å for Y-Cl. The Debye-Waller factor were calculated following equations in section 2.3 in Campbell et al. (1999).

Table 2. simulation details of ab initio MD

2.2 *Ab initio* thermodynamic integration

The *ab initio* MD results reveal the structure of Y(III)-Cl complexes at different P-T. However, *ab initio* MD is very resource-intensive: for example, obtaining 1 picosecond of real time data requires ~6,800 CPU hours for a simulation box containing 111 waters with density of 0.73 g/cm^3 at 450 ºC, and ~1,300 CPU hours for a simulation box containing 55 waters with density of 0.90 g/cm^3 at 350 ºC. This limits the timescale of MD simulations to 10's of picoseconds (ps). Under these conditions, observation of the distribution of species (i.e., statistical appraisal of association/dissociation reactions of ligands) in a solution can be beyond current computational capabilities, since ligand exchange rates are in the timescale of nanoseconds or microseconds for many aqua- and chloride complexes. For example, the water residence time of Ho^{3+} is 4.67 ns at 298 K (Cossy et al., 1989), with Y^{3+} expected to have a value within the same order of magnitude based on similarities in the ionic radius of Y(III) and Ho(III) (Shannon, 1979). The residence times of the Cl^- ligand in complexes of the transition metals Au(III), Zn(II) and Cd(II) are around 9.3 ms, 251 µs and <32 µs, respectively (Sharps et al., 1993). Even though ligand residence times decrease with temperature to a point where individual ligand exchange reactions can be easily observed via *ab initio* MD, the exchange rates are generally not sufficient to allow measurements of the relative complexes stabilities from the distribution of species in the simulations. Instead, the thermodynamic integration method (Sprik, 1998; Sprik & Ciccotti, 1998) was used to obtain

quantitative thermodynamic information on ligand exchange reactions. In this method, the limits imposed by the slow exchange kinetics in most ligand exchange reactions are lifted by measuring the free energy difference in the ligand exchange reaction along a user-defined reaction path, taking advantage of the fact that this energy difference is independent of the chosen reaction path. The method implementation is similar to that used by Mei et al. (2013a), and only a short summary is provided here; specific details of employing thermodynamic integration to calculate formation constant of Y(III) chloride complexes are described in section 3.4. We chose to investigate the chloride dissociation reactions, i.e.

$$YCl_n^{2+} = YCl_{n-1}^{3+} + Cl^- \quad (n=1\text{-}4) \qquad (1)$$

The reaction paths were defined by constraining the Y(III)-Cl distances (r) step-wise along coordinates that vary from the equilibrium bond (distance r_I) to a distance where the Cl^- ion does not interact with the complex (bulk distance, r_{II}). The mean constraint force ($f(r)$) required to maintain the Y(III)-Cl distance at r was obtained at each step. At each distance r, the simulation was conducted for at least 6 ps to sample a significant ensemble of possible configurations of Y(III)-Cl complexes and the surrounding solvent. The Helmholtz free energy of the ligand exchange reaction ($\Delta A_{I\rightarrow II}$) was retrieved by integrating $f(r)$ over the constrained distance (r_I to r_{II}) (Sprik et al., 1998; Sprik &Michiel, 2000):

$$\Delta A_{I\rightarrow II} = -\int_{r_I}^{r_{II}} f(r)dr \qquad (2)$$

The Helmholtz and Gibbs free energies are related by

$$\Delta_r G = \Delta A_{I \to II} + V \int_{P_0}^{P} dP \qquad (3)$$

where V is the volume of the box and $\int_{P_0}^{P} dP$ is the energy contribution due to the pressure change associated with the ligand exchange at constant volume. As shown in our previous work (Mei et al. 2013a), the contribution of $\int_{P_0}^{P} dP$ is small and thus is neglected. The standard Gibbs free energies of reactions ($\Delta_r G^{\Theta}$) were calculated from the Gibbs free energy of reactions ($\Delta_r G$) using

$$\Delta_r G^{\Theta} = \Delta_r G + RT \ln \frac{C_A \gamma_A \cdot C_B \gamma_B}{C_C \gamma_C \cdot C_D \gamma_D} \qquad (4)$$

where c_i are the concentration of the compounds of reaction A + B $\rightarrow$ C+ D, and γ_i are the activity coefficients of each species. By assuming $\gamma_i = 1$the Gibbs free energy of reactions of ideal solution ($\Delta_r G^{\Theta,c}$) were obtained. However, in this work, all simulations were conducted with high relatively concentrations (i.e. 3 m Cl^- and 5 m Cl^-) and high ionic strengths. The activity coefficients of the ions involved in the ligand exchange reactions were estimated with the B-dot extension of Debye-Hückel theory (Helgeson, 1981):

$$\log \gamma_i = -\frac{z_i^2 A_\gamma I^{1/2}}{1 + a_i B_\gamma I^{1/2}} + \dot{B}_\gamma I \qquad (5)$$

where z_i is the charge of ion i; I is the ionic strength in molality; a_i is the ion size parameter (Å); A_γ and B_γ are defined in Tables 1 and 2 in Helgeson and Kirkham (1974), $\dot{B}_\gamma$ is an empirical parameter taken from Oelkers and Helgeson (1990). Finally, the formation constants (K^{Θ}) for the ligand exchange reactions were calculated from

$$\Delta_r G^{\Theta} = -\mathrm{RT} \ln K^{\Theta} \qquad (6)$$

where R is the gas constant and T is temperature in Kelvin.

The uncertainties of the Gibbs free energies and $\log K^{\Theta}$ values in *ab initio* thermodynamic integrations were estimated with the method proposed by Allen and Tildesley (1987). This method has been used by Rodinger et al. (2005) and Mei et al. (2018) to estimate the uncertainty of thermodynamic integration. The statistical error of each mean constraint force ($\Delta f(r)$) was calculated as the standard deviation of the mean force divided by a statistical inefficiency coefficient; this error includes both the systematic and statistical errors (detail in section 6.4 in Allen and Tildesley, 1987). The statistical error of $\Delta_r G$ and $\log K^{\Theta}$ are obtained by accumulating $\Delta f(r)$over distance ($-\int_{r_I}^{r_{II}} \Delta f(r) dr$). The error of cumulative formation constant was measured using standard propagation rules.

2.3 Thermodynamic properties

To obtain the formation constants of Y(III)-Cl complexes over a broad temperature and pressure range, we fitted the MD calculation results with the modified Ryzhenko–Bryzgalin (MRB) model (Ryzhenko et al., 1985):

$$\log K_{(T,P)} = -\frac{T_r}{T}\log K_{(T_r,P_r)} + B_{(T,P)}\left(A_{(zz/a)} + \frac{B_{(zz/a)}}{T}\right) \qquad (7)$$

where K is the formation constant of Y(III)-Cl^- complexes at certain T and P; T_r, P_r are the reference temperature and pressure (*i.e.*, 25 ºC and 1 bar), and $A_{(zz/a)}$ and $B_{(zz/a)}$ are fitted empirical parameters (Shvarov and Bastrakov, 1999). The $B_{(T, P)}$ parameter is a species-independent function computed from the dissociation constant of water from Marshall and Franck (1981) (equation (2)). The fitting was done using the

OptimC code developed by Shvarov (2008, 2015). The modeling of speciation was conducted using the Matlab code BeerOz (Brugger, 2007).

2.4 XAS measurements and data processing

Experimental solutions for XAS measurements were prepared by dissolving the appropriate amounts of solids in acidified water. The compositions of the solutions are listed in Table 3. Analytical grade yttrium chloride (YCl_3•$6H_2O$), LiCl, NaCl, 37% HCl and MilliQ water were used to prepare the solutions.

Table 3. XAS solution

The speciation of yttrium in Cl-rich fluids was characterised via *in-situ* X-ray absorption measurements (XAS) using the high temperature-high pressure cell developed at the Institut Neel/ESRF (Bruyère et al., 2008; Testemale et al., 2005). This cell consists of an external water-cooled pressure vessel equipped with three beryllium windows enabling collection of simultaneous fluorescence and transmission signals. The sample is contained inside a glassy carbon tube with an internal diameter of 4 mm that is placed inside a small cylindrical resistive heater. Pressure is applied to the sample by two glassy carbon pistons, using helium as a pressure medium, while temperature is recorded by two thermocouples placed within the heating element. Although the thermocouple sits near the sample, it is placed outside the sample and the temperature of the fluid at the beam location needs to be calibrated (e.g., Brugger et al., 2007; Etschmann et al., 2010; Liu et al., 2011; Louvel et al., 2017). To do so,

286 the density of pure water is calculated from measurements of the absorbance and
287 X-ray mass attenuation coefficients tabulated by Chantler (1995), and then compared
288 to that from the equation of state of pure water (NIST database, Lemmon et al., 2000).
289 This method provides a direct measurement of the temperature at the beam position;
290 temperature accuracy is better than 5 ºC, and temperature varied within less that 1 ºC
291 during the measurements. Pressure was read from a calibrated Bourdin gauge with a
292 precision better than 5 bars; during the experiment, pressure was maintained with
293 1 bar by the PID system (Bruyère et al., 2008).

294 Yttrium K-edge (17,038 eV) X-ray Absorption Near Edge Structure (XANES)
295 and Extended X-ray Absorption Fine Structure (EXAFS) spectra were collected up to
296 500 ºC at 800 bars at the FAME beamline at the European Synchrotron Research
297 Facility (ESRF) in Grenoble, France. The ESRF is a 6.03 GeV ring, and operating in
298 7/8 multi-bunch mode it has a maximum current of 200 mA. FAME is a bending
299 magnet beamline (see Proux et al., 2005 for details), and its double crystal Si(220)
300 monochromator provides an energy resolution of 0.87 eV at the Y K edge energy. A
301 focused beam size of FWHM 220 x 145 μm^2 was used. The incident and transmitted
302 beam intensities I_0 and I_1 were measured with Si diodes, and a Canberra 30 element
303 solid state fluorescence detector was used for detecting fluorescence data. The beam
304 energy was calibrated with an Y foil, such that the maximum of the first derivative
305 was at 17,038 eV.

306 XANES and EXAFS data were analysed with the HORAE package (Ravel and

Newville, 2005), using FEFF version 9 (Rehr et al., 2009); E_0 was defined as the maximum of the first derivative. Reported errors in EXAFS parameters (1-σ) are those calculated by the Artemis program (part of HORAE).

2.5 ab initio XANES simulation

Ab initio XANES simulations were conducted using the FDMNES program (Joly, 2001; Joly et al., 2009) following the method described in previous studies of metal complexing (Testemale et al., 2009; Tian et al., 2014; Etschmann et al., 2018). The photo absorption cross sections were calculated using the Finite Difference Method (FDM), which is allows accurate calculations especially in the case of low-symmetry structures compared to methods based on the Muffin-Tin approximation, but at a cost of increased computing resources (Joly, 2001; Brugger, et al., 2007). To compare with the experimental spectra, the calculations were convoluted with a Lorentzian function of energy-dependent width to reproduce the core-hole lifetime broadening (3.52 eV; Krause and Oliver, 1979) and the inelastic plasmon interactions with the photoelectron. A Gaussian function (width of 0.87 eV) was employed to account for the energy resolution of the beamline at the convolution. In this study, theoretical spectra were calculated for: 1) crystalline Y_2O_3 solid (Santos et al., 2005), as a reference to estimate the accuracy of the simulations; 2) regular predefined square antiprism structures YO_8; 3) regular triangular antiprism structures and selected representative Y-O-Cl complexes (with total coordination of 6) from MD calculation at each condition (Figure 1a,c,d,e); 4) average of at least 50 MD whole

boxes at each condition. The radius cutoffs of all calculations were 5 Å.

3. Results

3.1 Geometrical properties from *ab initio* MD

Unconstrained MD simulations were performed in four solutions with different concentrations of Cl^- (Table 2) at 25 ºC, 200 ºC, 350 ºC, 450 ºC and 500 ºC. The simulation results are summarized in Table 4. The snapshots of different Y(III)-Cl^- complexes and pair distribution functions of Y-O and Y-Cl of each solutions are shown in Figure 1 and 2.

Table 4. simulation results from *ab initio* MD

Figure 1. snapshots of Y(III)-Cl

Figure 2. RDF

In box 1 (Y:Cl = 1:3), at ambient conditions (25 ºC, 1 bar), two jobs were conducted to test the stability of Y(III)-Cl complexes. In job 1a(1), the simulation started with $[Y(OH_2)_8]^{3+}$, and this configuration remained stable during the whole simulation. In job 1a(2), the initial configuration was $[Y(OH_2)_7Cl]^{2+}$ and Cl^- dissociated from Y(III) in less than 1 ps (Fig. 3a), and $[Y(OH_2)_8]^{3+}$ remained stable for the rest of the simulation. The eight water molecules in the first shell of Y^{3+} formed an antiprism structure (Fig. 1a, 1b), which is consistent with previous MD and XANES studies (Table 1). The Y-O bond distance (2.42 Å) from MD is also within the range of values from literature (2.36 Å to 2.51 Å, reference in Table 1), and close to our XAS results (2.37 to 2.39 Å, section 3.2). No evidence of Cl^-

bonding with Y(III) was found for this Cl concentration. The oscillations of Y-O bond distance indicate Debye-Waller factors of 0.0106 $Å^2$ and 0.0107 $Å^2$ for job 1a(1) and 1a(2), respectively.

Simulation 1b was run at 200 ºC and 800 bar for a total of 30.17 ps, starting with the $[Y(OH_2)_6Cl_2]^+$ complex as the initial configuration. The calculated hydration number is 5.2. One Cl^- dissociated from Y(III) from 14.6 ps to 22.6 ps (Fig. 3b), which leads to an average chloride coordination number of 1.8 over the simulation time. The RDFs in Fig. 2 indicate Y-Cl and Y-O bond distances of 2.65 Å and 2.36 Å, respectively. At 350 ºC, 800 bar (simulation 1c), the total coordination number of Y(III) further decrease to 6.5. Two water molecules bonded with Y(III) in the initial configuration detached from Y(III) within the first picosecond. The two Cl^- remained bonded to Y(III) at an average distance of 2.62 Å over the 23.87 ps simulation, *i.e.* no ligand change was observed. At 500 ºC, 800 bar and 1000 bar (simulation 1d and 1e), the final species was $[Y(OH_2)_5Cl_3]^0$. The Y-Cl and Y-O bond lengths (Fig. 2) were 2.55 – 2.56 Å and 2.44 Å, respectively.

Figure 3. Y-Cl distance over time

Simulations of box 2, 3, 4 were conducted with different Cl^- concentrations (Y:Cl = 1:4, 1:5, 1:2.5), and run at the same P-T conditions as box 1except room temperature. The bond distances and total coordination numbers calculated within each box are consistent at each P-T condition (Table 2). At 200 ºC, the coordination of Cl^- in box 4a is 1, whereas it is ~2 in the other boxes, suggesting an effect of

increasing Cl contents on the stability of Y-Cl complexes. At 500 ºC, 1000 bar, coordination of Cl^- is 2 for simulation 2c. In simulation 4c (Cl^- concentration of 5 m), at 450 ºC, 800 bar, the initial complex $[Y(OH_2)_5Cl_3]^0$ lost two waters within the first 1.5 ps, and became $[Y(OH_2)_3Cl_3]^0$, which remained stable for the last 15.41 ps. Interestingly, the coordination number of Cl^- reaches 4 in simulation 3c (Y:Cl = 1:5; 500 ºC, 1000 bar), with the average number of water molecules down to 1.7.

In general, the total coordination number decreases from 8 to 6 and Y(III)-Cl^- complexes become more stable as temperature increases from 25 ºC to 500 ºC. At high temperature (500 ºC), more chlorides are coordinated with Y(III) and hydration number decreases with more Cl^- complexes for a given P-T condition, different complexes were observed from MD simulations in each box. This reflects the different Y:Cl ratios in the boxes, but also the fact that the simulations in each box at the same P-T condition were started from different initial configurations, and due to the short time range of MD relative to ligand exchange rates, the final species detected from MD could be meta-stable.

3.2 XAS data refinement

3.2.1 XANES

XANES spectra are mainly a function of the oxidation state of the target atom, and the atomic number (e.g. O versus Cl) and geometrical arrangement of the ligands coordinated to the target atom. The edge position (red-shifted as the formal charge on the target atom decreases) and intensity of the white line (most intense band at the

edge position) can change as the ligands vary depending on composition and temperature (Bunker, 2010, Penner-Hahn, 2005; Etschmann, et al., 2017).

Yttrium XANES spectra show the classic "dehydration" effect with increasing temperature and salinity (e.g. Brugger et al., 2016). This is reflected by a decrease of the white line intensity and a shift to lower energy of the edge position, as shown in Figure 4 where the spectra obtained on Sol3 (0.01 m YCl_3) and Sol5 (9.5 m LiCl + 0.5 m HCl) at 25 and 400 ºC are compared. The effect of increasing temperature and salinity combine so that the decrease of the white line intensity and energy shift are more pronounced for Cl-rich Sol5. Note that that the small energy shift is more clearly observed in the first derivative of the XANES spectra (Fig 4(b)).

Figure 4. XANES on highest Cl solutions

The qualitative discussion above was supported using *ab initio* XANES simulations. As shown in Figure 6(a), the positions of the spectral features are well reproduced by the calculations for the Y_2O_3(s) standard, except for the band at ~65.9 eV, which is shifted by ~8 eV. The relative intensities are well reproduced, but the total intensity of the white line is lower in the simulations than in the experiments. Figure 6(b) explores the shifts of the spectral features resulting from changes in bond distance and angles in a high symmetry [YO_8] moiety. The angle affects the shape of the white line (intensity ratio of the two main bands contributing to the white line), and the bond distance causes a shift in the position of the white line. The MD structures -and most likely the real species in solution- reflect dynamic distortions of

412 the antiprism structure, which results in the small but significant differences in
413 calculated XANES spectra (Figure 6(c)). In order to account for this, we calculated
414 the averages from ≥50 frames over the simulation times for a number of simulations
415 (Figure 6(d)). In general, the results of FDMNES of MD boxes and experiments agree.
416 Importantly, the effects of temperature and salinity on the spectra are well reproduced
417 by the simulations. It is noticeable that the Y-O distance at room temperature from
418 MD and XAS is 2.42 Å and 2.37 Å, respectively; therefore, minor discrepancies
419 between the spectra from FDMNES of MD boxes and spectra from experiments are
420 reasonable.

421 Figure 6. XANES from FDMNES.

422 ### *3.2.2* EXAFS

423 EXAFS spectra represent a final state interference effect arising from the
424 scattering of the outgoing photoelectron from neighboring atoms, and are therefore
425 mainly sensitive to the nature (atomic number), quantity and distance of the
426 neighboring atoms.

427 The amplitude reduction factor (S_0^2) accounts for processes that contribute to
428 the X-ray absorption coefficient but not to the EXAFS (Roy et al. 1997), and is
429 determined by fitting a compound with similar molecular structure as the unknown. In
430 our case, S_0^2 was determined by fixing the coordination of a low salinity solution,
431 Sol6 (0.75 m HCl) at 30 ºC to eight oxygen atoms, because the structure of the Y(III)
432 aqua ion has been well characterized by previous studies (Ikeda et al., 2005a; Ohta et

al., 2008; Liu, X. et al., 2012; Lindqvist-Reis et al., 2000). A S_0^2 value of 0.73 was determined by refining the S_0^2, bond lengths and EXAFS Debye-Waller factors for this solution; this value is consistent with theoretical constraints (Roy et al. 1997) and was used in all subsequent refinements.

The YOCl(s) structure (Zachariasen, 1949, ICSD # 31667) was used to generate the O and Cl paths. For each solution, all spectra were fitted simultaneously, resulting in one ΔE_0 and one set of goodness-of-fit parameters for each solution (Table 5). The total ligand number (one oxygen path and one chlorine path) was restrained to be between 6 and 8; attempts to decrease the minimum coordination number to 5 resulted in statistically inferior fits. The Debye-Waller σ^2 was fitted at 25 ºC for each solution, with the constraint that it should then double from 30 to 500 ºC, as determined from MD simulations. Note that the Debye-Waller values determined from the *ab initio* MD simulations are higher than the experimental ones, as a result of the short sampling times in *ab initio* MD, that tend to overestimate structural disorder. However, the *relative* changes in fitted Debye-Waller values are likely to be accurate, especially since the vibrational characteristics of the complexes are well reproduced by *ab initio* MD (e.g. Mei et al. 2013b and references therein). In practice this was applied by increasing the EXAFS Debye-Waller by a factor of 1.2 for each ~100 ºC increase in temperature. The EXAFS Debye-Waller for Cl^- was defined to be the same as that for O, in part to reduce the number of variables and in part due to the (usually) low Cl:O ratio.

The Y k-space and Fourier transformed (R-space) EXAFS data are shown in Figure 5 and the fit results are tabulated in Table 5. As a general rule, the data show a small shift in k-space with increasing temperature. In R-space, the magnitude of the peak in the radial distribution function decreases, and the peak position shifts to a longer distance with increasing temperature, consistent with decreasing total coordination numbers and increasing Cl:O ratio. This evolution is also seen in the fitted structural parameters (Table 5): the largest change is recorded in Sol5 (9.5 m LiCl+0.5 m HCl), where the total ligand number decreased from 7.6 (30 ºC) to 6.0 (450 ºC), with the Cl:O ratio increasing from 0.0 to 1.0. Attempts were made to increase the Cl:O ratio to 2, i.e. 4xCl+2xO, in-line with the results from MD, however this skewed the fit peak significantly, resulting in a poor overall fit to the data.

Figure 5. EXAFS

Table 5 EXAFS result

In contrast, the total coordination number does not decrease as much in low salinity solutions, e.g. from 8 to 7 (Sol3, 30 to 400 ºC) and 8 to 7.7 (Sol6, 30 to 400 ºC), while the Cl:O ratio increases from 0 to ~0.6 and ~0.4 (Sol6 and Sol3 respectively).

3.3 Estimating formation constants by *ab initio* thermodynamic integration

The MD simulations described above provided qualitative information about the nature and geometry of the Y-Cl complexes in chloride solutions to 500 ºC. However,

thermodynamic properties of Y-Cl complexes are necessary to determine their relative stabilities and the mobility of Y(III) under hydrothermal conditions.

Figure 7. FES of YCl^{2+}

Figure 7 shows an example of employing *ab initio* MD to calculate the free energy surface of the reaction:

$$YCl^{2+} = Y^{3+} + Cl^{-} \qquad (8)$$

The Helmholtz free energy $\Delta A_{I \to II}$ of reaction (8) was calculated by integrating the constraint mean force (*f(r)*) between Y^{3+} and Cl^{-} (equation (1)) from the equilibrium position (2.65 Å), which corresponds to the equilibrated Y(III)-Cl^{-} bond distance in the previous unconstraint MD simulations, to a non-interacting position (6.00 Å). An external force is required to eliminate the interactions between Y^{3+} and Cl^{-} to maintain the targeted Y(III)-Cl^{-} distance. When the Y(III)-Cl^{-} distance was between 3.1 Å and 3.55 Å, the absolute value of *f(r)* varied from zero to a minimum of -45.14 kJ/mol•Å to near zero (3.32 kJ/mol•Å), and the free energy reached it maximum (23.50 kJ/mol), which means at this stage, one water molecule associated with yttrium, i.e. reaction (7) results in the replacement of one chloride ion by one water molecule. The mean constraint forces become positive are positive at distances between 3.4 Å and 5.4 Å, which reflects the activation barrier of the ion exchange reaction. It can be seen from Figure 7 that when the Y(III)-Cl^{-} distance is beyond 4.5 Å, the constraint mean force is very small (9.01 kJ/mol•Å, 2.03 kJ/mol•Å, -2.69 kJ/mol•Å, and -9.45 kJ/mol•Å at distances of 4.5 Å, 4.9 Å, 5.4 Å, and 6 Å, respectively), as expected as chloride-Y(III)

interaction become vanishingly small. The integration of the Y(III)-Cl^- mean constraint force over the reaction path gives a free energy for reaction (7) of 3.92 ± 8.85 kJ/mol.

Figure 8. free energy surface of all calculation

Figure 8 shows the free energy surface of the stepwise dissociation of Y(III)-chloride complexes in solutions with different Cl^- concentrations (box 1 and 3) at 200 ºC, 800 bar; 350 ºC, 800 bar; and 500 ºC, 1000 bar. In order to achieve good sampling of the constraint force, one more free chloride was set in the system at a far distance (6 Å) to conduct thermodynamic integration, i.e. in box 1, which contains three Cl^-, the free energies of formation of YCl_n^{3-n} complexes were calculated only when n=1 and 2; in box 3, which contains five Cl^-, $\Delta_r G$ of YCl_n^{3-n} (n = 1,2,3,4) were measured (Table 6).

Table 6. ΔG and $\log K^{\Theta}$ of two boxes

Comparing results from box 1 and box 3, the calculated $\Delta_r G$ for the association reactions of YCl^{2+} and YCl_2^+ vary because of the difference of Cl^- activity in each box. After activity correction, the value of standard Gibbs free energies ($\Delta_r G^{\Theta}$) of each ligand exchange reaction were close (four are ≤2.2 kJ/mol, and two ≤3.8 kJ/mol) at the same P-T condition. The stepwise formation constants, $\log K^{\Theta}$, that were obtained from the two boxes at each P-T condition, their errors and averages are presented in Figure 9. The consistency of the two $\log K^{\Theta}$ values from the two boxes validates the thermodynamic integration method for calculating the energetics of these ligand

exchange reactions, demonstrating that the values do not depend on the composition or size of the simulation box, and that the sampling time of the simulations is sufficient. In this study, we take the average stepwise formation constant of the two boxes as the final stepwise formation constant of the YCl^{2+} and YCl_2^{+} association reactions at 200 ºC, 800 bar; 350 ºC, 800 bar; and 500 ºC, 1000 bar. The error of the average formation constant was measured using the standard propagation rules. The stepwise ($\log K^{\Theta}$) and cumulative ($\log\beta^{\Theta}$) formation constants of Y(III)-chloride complexes are summarized in Tables 6 and 7, respectively.

Figure 9. average $\log K^{\Theta}$ and each $\log K^{\Theta}$ within error bar in different boxes with T.

Table 7. *logβ* of Y(III)-Cl.

The calculated *logβ* in Table 7 are employed to fit the modified MRB model (eq. 6) to extrapolate the formation constant of Y(III)-Cl^- associate reactions to higher temperature and pressure. We fit two parameters in equation (6) for each species to minimize the uncertainties. The $log\beta^{\Theta}_{(25^{\circ}C,1\ bar)}$ of YCl^{2+} was chosen from Luo & Byrne (2001), which is the only available experiment data of Y(III)-Cl complexes, two parameters (*A* and *B)* were fitted; but for YCl_2^{+}, YCl_3, and YCl_4^{-}, the $B_{(zz/a)}$ are set to zero, and $log\beta^{\Theta}_{(25^{\circ}C,1\ bar)}$ and the *A* parameter were fitted. The fitted MRB parameters are listed in Table 8. The extrapolated logarithm of formation constants of Y(III)-Cl complexes at 25 ºC to 500 ºC, saturated pressure (P_{sat}) to 5000 bar from MRB, are listed in Table 9.

Table 8. MRB parameters

Table 9. logβ from MRB

4 Discussion

4.1 Stability of Y(III)-Cl complexes

In general, the speciation derived from the unconstrained MD (section 3.1) agrees well with XAS fits (section 3.2) (Figures 10 and 11). The XANES spectra calculated from *first principles* from the MD simulations reproduce the experimental spectral features and their changes with temperature and salinity well (Figure 6d). The experiments and theoretical approaches both reveal the same trends of Y(III)-Cl complexes along with temperature, with more Cl^- bonding with Y(III) at high temperatures.

Figure 10. Coordination of O and Cl from XAS and MD

The formation constants obtained from thermodynamic integration enable us to predict Y(III)-Cl^- speciation at different PT and Cl^- concentrations and provide the first self-consistent speciation model for Y(III) chloride complexing from room-temperature to high-temperature hydrothermal conditions. The results indicate that the formation of Y(III)-chloride complexes can affect the mobility of yttrium under hydrothermal conditions and also the distribution of REE elements in REE deposits.

Figure 11 shows the distribution of Y(III) chloride complexes at different T, P and pH, as a function of total chloride in the solution. The number of coordinated chloride ligands from XAS Sol3 (0.03 m Cl^-), Sol5 (2.5 m Cl^-) and Sol7 (5 m Cl^-) are

559 also plotted in Figures 11a,c and 11d,e,f for comparison (right axis, orange dots). At
560 200 ºC and $pH_{200ºC}$ =0.3 and 3, the hydrated Y^{3+} ion remains the dominant form of
561 Y(III) even in high salinity solutions (Figure 11a,b). At 350 ºC, the stability of the
562 different species not only varies with Cl^- concentrations, but also with pH, so that the
563 predominant species remains $YCl_3(aq)$ from $n(Cl^-) > 0.4$ m at $pH_{350ºC} = 0.3$, but
564 changes to YCl_4^- at $pH_{350ºC} = 3$. At 500 ºC, 1000 bar (Figure 11e,f), the dominant
565 species is YCl_4^- for $pH_{350ºC}$ =3, and $YCl_3(aq)$ for $pH_{350ºC} = 0.3$. The coordination
566 number of Cl^- is also 3 in XAS Sol 5 at 450 ˚C, whose Cl^- concentration is 10 m but
567 also with high acidity. This decrease of Cl neighbors is likely due to the association of
568 HCl at high temperature (Mei et al., 2018; Tagirov et al., 1997) that leaves less free
569 Cl^- available to bond with Y(III) in very acidic solutions.

570 While the general trends defined by (i) XAS, (ii) unconstrained MD (Figure 10)
571 and (iii) thermodynamic modelling (Figure 11) derived from thermodynamic
572 integration are consistent with each other, small discrepancies in the coordination
573 number between the methods are noticeable. For example, at 200 ºC, both
574 unconstrained MD and the thermodynamic model indicate that there are Cl^-
575 bonding with Y(III) when $n(Cl^-) > 2.5$ m (1 to 2 in MD and ~0.5 in the
576 thermodynamic model), whereas XAS analysis reveals very minor chlorine
577 complexation in Sol 7 and no chlorine complexation in Sol 6 (Table 5 Sol6) (i.e.,
578 below detection limit of ~ 0.3 Cl^-). At 350 ºC, the thermodynamic model suggests
579 higher order Y(III)-Cl species than MD and XAS. This is because:

(1) thermodynamic integration with the MD method tends to overestimate the formation constants of complexes, and especially higher order complexes, at relative low temperature due to the low kinetic energy of the ions and water molecules, resulting in poor sampling of the force (Mei, et al., 2018). This translates into larger errors on the $log\beta$ values at 25 ºC than at 300 ºC, for example (Mei et al., 2013a, 2015a). Therefore, the $log\beta$ of Y(III)-Cl species at 200 and 350 ºC from MD that was employed to model Y(III)-Cl distribution in this study could still be higher than actual, and consequently leads to the overestimation of the coordination of Y(III)-Cl. (2) As discussed above, due to the limits of CPU resources, the simulation time of unconstrained MD is not sufficient to observe the stable species, so species reported in Figure 10 could be meta-stable. (3) The experimental solutions are more acidic than those in the simulations, and HCl association could explain the lower Y-Cl bonding compared to other solutions and to the MD simulations (Fig. 11).

Overall, Y(III) mobility in hydrothermal conditions is expected to increase because of the increased stability of higher-order Y(III)-Cl with increasing temperature and Cl^- concentration.

Figure 11. Y-Cl species with n(Cl^-) at different T and pH

4.2 REE-Cl^- complexation in hydrothermal fluids

The Y^{3+} ionic radius is close to that of Ho^{3+}, and Y has consequently frequently been grouped with heavy REE. However, differences in their aqueous speciation has

601 the potential to lead to different mobility of the REE and Y in natural hydrothermal
602 systems. Up to now, this possibility could not be investigated due to the lack of
603 thermodynamic properties for Y(III)-Cl complexes (Migdisov et al., 2016). The
604 formation constants of YCl^{2+} and YCl_2^{+} at 150, 200 and 250 ºC, and P_{sat} have been
605 derived from the fitted MRB parameters of Y(III)-Cl complexes (Table 9) and can
606 now be compared to other REE data (Table 1, Migdisov et al., 2009) (Figure 12). At
607 150 ºC, the formation constant for YCl^{2+} is close to zero, much smaller than those
608 reported by Midgisov et al. (2016) for $REECl^{2+}$, even when considering the heaviest
609 REE (Lu, which is 1.14). At 200 ºC, yttrium behaves similar to the heavy REE
610 (HREE) element (Lu) in Cl-rich solutions. In this condition, the LREE are more stable
611 in solution and mobile than HREE, including Y(III). Nevertheless, the formation
612 constants of Y-Cl complexes increase faster than those of other HREE with increasing
613 temperature, so that at 250 ºC Y(III)-Cl complexes are more stable than HREE, and Y
614 behaves more like the LREE (La).

615 Figure 12. Compare of $log\beta$ of REE & Y values

616 Differences between Y and the HREE thermodynamics under hydrothermal
617 conditions provide a likely explanation for the fractionation of Y from Ho reported in
618 some hydrothermal REE minerals (Bau and Dulski, 1995). The distribution of Ho(III)
619 and Y(III) species as a function of Cl^- concentration at 250 ºC, P_{sat} are presented in
620 Figure 13, with the data presented in Table 9 for Y(III) and measured by Migdisov et
621 al (2009) for Ho^{3+}, $HoCl_2^{+}$ and $HoCl^{2+}$, and predicted from Haas et al. (1995) for

$HoCl_3$(aq). As thermodynamic data for Ho(III) are only available until trichloro complexes, YCl_4^- is not considered in Figure 13. At 250 ºC, the dominant species for Y(III) in Cl-bearing solution is YCl_2^+, whereas for Ho(III), it remains $HoCl^{2+}$ until Cl^- concentration reaches ~4.5 m and becomes $HoCl_2^+$ afterwards. Such slight differences could ultimately account for contrasting REE(Y) distribution in hydrothermal REE deposits. However, the minerals deposited from hydrothermal fluids contain many components, i.e. F^-, SO_4^{2-}, CO_3^{2-}. The behaviors of REE with most of these ligands are unclear but can affect the process of precipitation; therefore, further studies are required to quantitatively model how REE minerals deposits in hydrothermal process.

Figure 13. Y-Cl/Ho-Cl species distribution with Cl^- concentration at 250 ˚C, P_{sat}

Acknowledgements

We are grateful to the Australian Research Council (discovery grant DP190100216) for supporting this work. The MD part of this work was supported by resources provided by the Pawsey Supercomputing Centre with funding from the Australian Government and the Government of Western Australia and the high-performance computers in CSIRO. We are grateful to the European Synchrotron Research Facility (Grenoble, France) for providing beamtime, and to the Australian International Synchrotron Access Program (ISAP) managed by the Australian Synchrotron, part of ANSTO, and funded by the Australian Government, for travel funding. M. Louvel also acknowledges funding from the European Union's Horizon 2020 Marie Skłodowska-Curie grant DLV-797145.

Research data

Relevant research data are in attached spreadsheet.

References

Allen, M. and Tildesley, D. (1987) Computer Simulation of Liquids Oxford Univ. Press. Oxford.

Allen, P.G., Bucher, J.J., Shuh, D.K., Edelstein, N.M. and Craig, I. (2000) Coordination Chemistry of Trivalent Lanthanide and Actinide Ions in Dilute and Concentrated Chloride Solutions. Inorganic Chemistry 39, 595-601.

Bankura A., Karmakar A., Carnevale V., Chandra A. and Klein 1064 M. L. (2014) Structure, dynamics, and spectral diffusion of water from first-principles molecular dynamics. Journal of Physycal Chemistry 1066 C 118, 29401–29411.

Bau, D. (1995) Comparative study of yttrium and rare-earth element behaviours in fluorine-rich hydrothermal fluids. Contrib Mineral petrol 119, 213-223.

Becke, A.D. (1988) Density-functional exchange-energy approximation with correct asymptotic behavior. Phys. Rev. A 38, 3098-3100.

Bowron, D.T. and Diaz-Moreno, S. (2007) Local Structure Refinement of Disordered Material Models: Ion Pairing and Structure in YCl ₃ Aqueous Solutions. The Journal of Physical Chemistry B 111, 11393-11399.

Brugger, J. (2007a) BeerOz, a set of Matlab routines for the quantitative interpretation of spectrophotometric measurements of metal speciation in solution. Computers & Geosciences 33, 248-261.

Brugger, J., Etschmann, B., Liu, W., Testemale, D., Hazemann, J.-L., Emerich, H., Van Beek, W. and Proux, O. (2007b) An XAS study of the structure and thermodynamics of Cu (I) chloride complexes in brines up to high temperature (400 C, 600 bar). Geochimica et Cosmochimica Acta 71, 4920-4941.

Brugger, J., Etschmann, B., Pownceby, M., Liu, W., Grundler, P. and Brewe, D. (2008) Oxidation state of europium in scheelite: Tracking fluid–rock interaction in gold deposits. Chemical Geology 257, 26-33.

Brugger, J., Liu, W., Etschmann, B., Mei, Y., Sherman, D.M. and Testemale, D. (2016) A review of the coordination chemistry of hydrothermal systems, or do coordination changes make ore deposits? Chemical Geology 447, 219-253.

Bruyère, R., Prat, A., Goujon, C. and Hazemann, J.-L. (2008) A new pressure regulation device using high pressure isolation valves, Journal of Physics: Conference Series. IOP Publishing, p. 122003.

678 Bunker, G. (2010) Introduction to XAFS: a practical guide to X-ray absorption fine structure
679 spectroscopy. Cambridge University Press.

680 Bunău, O. and Joly, Y. (2012) Full potential x-ray absorption calculations using time
681 dependent density functional theory. Journal of Physics: Condensed Matter 24, 215502.

682 Campbell, L., Rehr, J.J., Schenter, G.K., McCarthy, M.I. and Dixon, D. (1999) XAFS
683 Debye–Waller factors in aqueous Cr+3 from molecular dynamics. Journal of
684 Synchrotron Radiation 6, 310-312.

685 Car, R. and Parrinello, M. (1985) Unified Approach for Molecular Dynamics and
686 Density-Functional Theory. Phys. Rev. Lett. 55, 2471-2474.

687 Chantler, C.T. (1995) Theoretical form factor, attenuation, and scattering tabulation for Z=
688 1–92 from E= 1–10 eV to E= 0.4–1.0 MeV. Journal of Physical and Chemical Reference
689 Data 24, 71-643.

690 Cossy, C., Helm, L. and Merbach, A.E. (1989) High-pressure NMR study. 38.
691 Water-exchange mechanisms on the terbium to thulium octaaqualanthanide(III) ions: a
692 variable-pressure oxygen-17 NMR study. Inorganic Chemistry 28, 2699-2703.

693 D'Angelo, P. and Spezia, R. (2012) Hydration of lanthanoids(III) and actinoids(III): an
694 experimental/theoretical saga. Chemistry 18, 11162-11178.

695 Díaz-Moreno, S., Muñoz-Páez, A. and Chaboy, J. (2000) X-ray Absorption Spectroscopy
696 (XAS) Study of the Hydration Structure of Yttrium(III) Cations in Liquid and Glassy
697 States: Eight or Nine-Fold Coordination? The Journal of Physical Chemistry A 104,
698 1278-1286.

699 Driesner, T. (2007) The system H2O–NaCl. Part II: Correlations for molar volume, enthalpy,
700 and isobaric heat capacity from 0 to 1000°C, 1 to 5000bar, and 0 to 1 XNaCl.
701 Geochimica et Cosmochimica Acta 71, 4902-4919.

702 Driesner, T. and Heinrich, C.A. (2007) The system H2O–NaCl. Part I: Correlation formulae
703 for phase relations in temperature–pressure–composition space from 0 to 1000°C, 0 to
704 5000bar, and 0 to 1 XNaCl. Geochimica et Cosmochimica Acta 71, 4880-4901.

705 Etschmann, B., Liu, W., Testemale, D., Mueller, H., Rae, N., Proux, O., Hazemann, J.-L. and
706 Brugger, J. (2010) An in situ XAS study of copper (I) transport as hydrosulfide
707 complexes in hydrothermal solutions (25–592 C, 180–600 bar): speciation and solubility
708 in vapor and liquid phases. Geochimica et Cosmochimica Acta 74, 4723-4739.

709 Etschmann, B., Liu, W., Li, K., Dai, S., Reith, F., Falconer, D., Kerr, G., Paterson, D.,
710 Howard, D. and Kappen, P. (2017) Enrichment of germanium and associated arsenic and
711 tungsten in coal and roll-front uranium deposits. Chemical Geology 463, 29-49.

712 Etschmann, B.E., Mei, Y., Liu, W., Sherman, D., Testemale, D., Müller, H., Rae, N., Kappen,
713 P. and Brugger, J. (2018) The role of Pb(II) complexes in hydrothermal mass transfer:
714 An X-ray absorption spectroscopic study. Chemical Geology 502, 88-106.

715 Etschmann, B., Liu, W., Mayanovic, R., Mei, Y., Heald, S., Gordon, R. and Brugger, J.
716 (2019) Zinc transport in hydrothermal fluids: On the roles of pressure and sulfur vs.
717 chlorine complexing. American Mineralogist 104, 158-161.

718 Gammons, C.H., Wood, S.A. and Williams-Jones, A.E. (1996) The aqueous geochemistry of
719 the rare earth elements and yttrium: VI. Stability of neodymium chloride complexes
720 from 25 to 300°C. Geochimica et Cosmochimica Acta 60, 4615-4630.

721 Gillan, M.J., Alfè, D. and Michaelides, A. (2016) Perspective: How good is DFT for water?
722 The Journal of Chemical Physics 144, 130901.

723 Gysi, A.P., Williams-Jones, A.E. and Harlov, D. (2015) The solubility of xenotime-(Y) and
724 other HREE phosphates (DyPO 4 , ErPO 4 and YbPO 4) in aqueous solutions from 100
725 to 250 °C and p sat. Chemical Geology 401, 83-95.

726 Helgeson, H.C. and Kirkham, D.H. (1974) Theoretical prediction of the thermodynamic
727 behavior of aqueous electrolytes at high pressures and temperatures; II, Debye-Huckel
728 parameters for activity coefficients and relative partial molal properties. American
729 Journal of Science 274, 1199-1261.

730 Helgeson, H.C., Kirkham, D.H. and Flowers, G.C. (1981) Theoretical prediction of the
731 thermodynamic behavior of aqueous electrolytes by high pressures and temperatures; IV,
732 Calculation of activity coefficients, osmotic coefficients, and apparent molal and
733 standard and relative partial molal properties to 600 degrees C and 5kb. American
734 Journal of Science 281, 1249-1516.

735 Helm, L. and Merbach, A.E. (2005) Inorganic and Bioinorganic Solvent Exchange
736 Mechanisms. Chem. Rev. 105, 1923-1960.

737 Humphrey, W., Dalke, A. and Schulten, K. (1996) VMD: Visual molecular dynamics. Journal
738 of Molecular Graphics 14, 33-38.

739 Ikeda, T., Hirata, M. and Kimura, T. (2005a) Hydration of Y3+ ion: A Car-Parrinello
740 molecular dynamics study. The Journal of Chemical Physics 122, 024510.

741 Ikeda, T., Hirata, M. and Kimura, T. (2005b) Hydration structure of Y 3+ and La 3+
742 compared: An application of metadynamics. The Journal of chemical physics 122,
743 244507.

744 Johansson, g. and Wakita, H. (1985) X-ray investigation of the coordination and complex
745 formation of lanthanoid ions in aqueous perchlorate and selenate solutions. Inorganic
746 Chemistry 24, 3047-3052.

747 Joly, Y. (2001) X-ray absorption near-edge structure calculations beyond the muffin-tin
748 approximation. Phys. Rev. B 63, 125120.

749 Joly, Y., Bunău, O., Lorenzo, J.E., Galéra, R.M., Grenier, S. and Thompson, B. (2009)
750 Self-consistency, spin-orbit and other advances in the FDMNES code to simulate
751 XANES and RXD experiments. Journal of Physics: Conference Series 190, 012007.

752 Kontonikas-Charos, A., Ciobanu, C.L., Cook, N.J., Ehrig, K., Ismail, R., Krneta, S. and Basak,
753 A. (2018) Feldspar mineralogy and rare-earth element (re)mobilization in iron-oxide

754 copper gold systems from South Australia: a nanoscale study. Mineral. mag. 82,
755 S173-S197.

756 Krause, M. O., & Oliver, J. H. (1979). Natural widths of atomic K and L levels, K α X- ray
757 lines and several KLL Auger lines. Journal of Physical and Chemical Reference
758 Data, 8(2), 329-338.

759 Krishnamurthy, N., Gupta, C.K. and Gupta, C.K. (2015) Extractive Metallurgy of Rare Earths.
760 CRC Press.

761 Lee, C., Yang, W. and Parr, R.G. (1988) Development of the Colle-Salvetti
762 correlation-energy formula into a functional of the electron density. Phys. Rev. B 37,
763 785-789.

764 Lemmon, E.W., McLinden, M.O. and Friend, D.G. (2000) Thermophysical properties of fluid
765 systems. National Institute of Standards and Technology, Gaithersberg.

766 Lin, I.C., Seitsonen, A.P., Tavernelli, I. and Rothlisberger, U. (2012) Structure and dynamics
767 of liquid water from ab initio molecular dynamics - comparison of BLYP, PBE and
768 revPBE density functionals with and without van der Waals corrections. Journal of
769 Chemical Theory and Computation 8, 3902-3910.

770 Lindqvist-Reis, P., Lamble, K., Pattanaik, S., Persson, I. and Sandström, M. (2000) Hydration
771 of the Yttrium(III) Ion in Aqueous Solution. An X-ray Diffraction and XAFS Structural
772 Study. The Journal of Physical Chemistry B 104, 402-408.

773 Ling, M.-X., Liu, Y.-L., Williams, I.S., Teng, F.-Z., Yang, X.-Y., Ding, X., Wei, G.-J., Xie,
774 L.-H., Deng, W.-F. and Sun, W.-D. (2013) Formation of the world's largest REE deposit
775 through protracted fluxing of carbonatite by subduction-derived fluids. Sci Rep 3, 1776.

776 Liu, W., Borg, S.J., Testemale, D., Etschmann, B., Hazemann, J.-L. and Brugger, J. (2011)
777 Speciation and thermodynamic properties for cobalt chloride complexes in hydrothermal
778 fluids at 35–440 C and 600 bar: an in-situ XAS study. Geochimica et Cosmochimica
779 Acta 75, 1227-1248.

780 Liu, X., Lu, X., Wang, R. and Zhou, H. (2012) First-principles molecular dynamics study of
781 stepwise hydrolysis reactions of Y3+ cations. Chemical Geology 334, 37-43.

782 Liu, W., Etschmann, B.E., Migdisov, A., Boukhalfa, H., Testemale, D., Muller, H., Hazemann,
783 J-L. and Brugger, J., 2017. Revisiting the hydrothermal geochemistry of europium
784 (II/III) in light of new in-situ XAS spectroscopy results. Chemical Geology 459, 61-74.

785 Loges, A., Migdisov, A.A., Wagner, T., Williams-Jones, A.E. and Markl, G. (2013) An
786 experimental study of the aqueous solubility and speciation of Y(III) fluoride at
787 temperatures up to 250°C. Geochimica et Cosmochimica Acta 123, 403-415.

788 Louvel, M., Bordage, A., Testemale, D., Zhou, L. and Mavrogenes, J., 2015. Hydrothermal
789 controls on the genesis of REE deposits: Insights from an in situ XAS study of Yb
790 solubility and speciation in high temperature fluids (T < 400 C). Chemical Geology
791 417, 228-237.

792 Louvel, M., Bordage, A., Tripoli, B., Testemale, D., Hazemann, J-L. and Mavrogenes, J.,
793 2017. Effect of S on the aqueous and gaseous transport of Cu in porphyry and

epithermal systems: Constraints from in situ XAS measurements up to 600 C and 300 bars. Chemical Geology 466, 500-511.

Luo, Y.-R. and Byrne, R.H. (2001) Yttrium and Rare Earth Element Complexation by Chloride Ions at 25◦C. Journal of Solution Chemistry, 9.

Marques, M.I.d.B., Marques, M.A. and Rodrigues, J.R. (1992) The structure of the first coordination shell of the yttrium ion in concentrated aqueous solutions of YBr ₃ and YCl ₃. Journal of Physics: Condensed Matter 4, 7679-7690.

Marshall, W.L. and Franck, E.U. (1981) Ion product of water substance, 0–1000 °C, 1–10,000 bars New International Formulation and its background. Journal of Physical and Chemical Reference Data 10, 295-304.

Matsubara, E., Okuda, K. and Waseda, Y. (1990) Anomalous X-ray scattering study of aqueous solutions of YCl ₃ and ErCl ₃. Journal of Physics: Condensed Matter 2, 9133-9143.

Mei, Y., Sherman, D.M., Liu, W. and Brugger, J. (2013a) *Ab initio* molecular dynamics simulation and free energy exploration of copper(I) complexation by chloride and bisulfide in hydrothermal fluids. Geochimica et Cosmochimica Acta 102, 45-64.

Mei, Y., Sherman, D.M., Liu, W. and Brugger, J. **(**2013b) Complexation of gold in S_3^--rich hydrothermal fluids: evidence from *ab-initio* molecular dynamics simulations. Chemical Geology, 347, 34–42.

Mei, Y., Sherman, D.M., Liu, W., Etschmann, B., Testemale, D. and Brugger, J. (2015a) Zinc complexation in chloride-rich hydrothermal fluids (25–600 °C): A thermodynamic model derived from *ab initio* molecular dynamics. Geochimica et Cosmochimica Acta 150, 265-284.

Mei, Y., Etschmann, B., Liu, W., Sherman, D.M., Barnes, S.J., Fiorentini, M.L., Seward, T.M., Testemale, D. and Brugger, J. (2015b) Palladium complexation in chloride- and bisulfide-rich fluids: Insights from ab initio molecular dynamics simulations and X-ray absorption spectroscopy. Geochimica et Cosmochimica Acta 161, 128-145.

Mei, Y., Etschmann, B., Liu, W., Sherman, D.M., Testemale, D. and Brugger, J. (2016) Speciation and thermodynamic properties of zinc in sulfur-rich hydrothermal fluids: Insights from ab initio molecular dynamics simulations and X-ray absorption spectroscopy. Geochimica et Cosmochimica Acta 179, 32-52.

Mei, Y., Liu, W., Brugger, J., Sherman, D.M. and Gale, J.D. (2018) The dissociation mechanism and thermodynamic properties of HCl(aq) in hydrothermal fluids (to 700 °C, 60 kbar) by ab initio molecular dynamics simulations. Geochimica et Cosmochimica Acta 226, 84-106.

Migdisov, A.A. and Williams-Jones, A.E. (2008) A spectrophotometric study of Nd(III), Sm(III) and Er(III) complexation in sulfate-bearing solutions at elevated temperatures. Geochimica Cosmochimica Acta 72, 5291-5303.

Migdisov, A.A., Williams-Jones, A.E., Normand, C. and Wood, S.A. (2008) A spectrophotometric study of samarium (III) speciation in chloride solutions at elevated temperatures. Geochimica Cosmochimica Acta 72, 1611-1625.

Migdisov, A., Williams-Jones, A.E., Brugger, J. and Caporuscio, F.A. (2016) Hydrothermal transport, deposition, and fractionation of the REE: Experimental data and thermodynamic calculations. Chemical Geology 439, 13-42.

Migdisov, A.A., Williams-Jones, A.E. and Wagner, T. (2009) An experimental study of the solubility and speciation of the Rare Earth Elements (III) in fluoride- and chloride-bearing aqueous solutions at temperatures up to 300°C. Geochimica et Cosmochimica Acta 73, 7087-7109.

Ohta, A., Kagi, H., Tsuno, H., Nomura, M. and Kawabe, I. (2008) Influence of multi-electron excitation on EXAFS spectroscopy of trivalent rare-earth ions and elucidation of change in hydration number through the series. American Mineralogist 93, 1384-1392.

Penner- Hahn, J.E. (2001) X- ray absorption spectroscopy. e LS.

Proux, O., Biquard, X., Lahera, E., Menthonnex, J.-J., Prat, A., Ulrich, O., Soldo, Y., Trévisson, P., Kapoujyan, G. and Perroux, G. (2005) FAME: A new beamline for X-ray absorption investigations of very-diluted systems of environmental, material and biological interests. Physica Scripta 2005, 970.

Ram, R., Becker, M., Brugger, J., Etschmann, B., Burcher-Jones, C., Howard, D., Kooyman, P. and Petersen, J. (2019) Characterisation of a rare earth element (REE)-bearing ion-adsorption clay deposit in Madagascar. Chemical Geology 522, 93-107.

Ravel, B. and Newville, M. (2005) ATHENA, ARTEMIS, HEPHAESTUS: data analysis for X-ray absorption spectroscopy using IFEFFIT. Journal of synchrotron radiation 12, 537-541.

Rehr, J.J., Kas, J.J., Prange, M.P., Sorini, A.P., Takimoto, Y. and Vila, F. (2009) Ab initio theory and calculations of X-ray spectra. Comptes Rendus Physique 10, 548-559.

Rodinger, T., Howell, P.L. and Pomès, R. (2005) Absolute free energy calculations by thermodynamic integration in four spatial dimensions. The Journal of chemical physics 123, 034104.

Roy, M., Gurman, S.J. and vanDorssen, G. (1997) The amplitude reduction factor in EXAFS. Journal De Physique Iv 7, 151-152.Rudolph, W.W. and Irmer, G. (2015) Hydration and ion pair formation in aqueous Y^{3+}–salt solutions. Dalton Transactions 44, 18492-18505.

Ryzhenko, B., Bryzgalin, O., Artamkina, I.Y., Spasennykh, M.Y. and Shapkin, A. (1985) An electrostatic model for the electrolytic dissociation of inorganic substances dissolved in water. Geochem. Int. 22, 138-144.

Santos, C., Strecker, K., Suzuki, P.A., Kycia, S., Silva, O.M.M. and Silva, C.R.M. (2005) Stabilization of α-SiAlONs using a rare-earth mixed oxide (RE2O3) as sintering additive. Materials Research Bulletin 40, 1094-1103.

871 Shannon, R.D. (1976) Revised effective ionic radii and systematic studies of interatomic
872 distances in halides and chalcogenides. Acta crystallographica section A: crystal physics,
873 diffraction, theoretical and general crystallography 32, 751-767.

874 Sharps, J.A., Brown Jr, G.E. and Stebbins, J.F. (1993) Kinetics and mechanism of ligand
875 exchange of Au (III), Zn (II), and Cd (II) chlorides in aqueous solution: An NMR study
876 from 28–98 C. Geochimica et cosmochimica acta 57, 721-731.

877 Shvarov, Y.V. and Bastrakov, E. (1999) HCh: a software package for geochemical
878 equilibrium modelling. User's Guide Record/25 (Australian Geological Survey
879 Organisation, Canberra, 1999).

880 Shvarov, Y.V. (2008) HCh: New potentialities for the thermodynamic simulation of
881 geochemical systems offered by windows. Geochem. Int. 46, 834-839.

882 Shvarov, Y. (2015) A suite of programs, OptimA, OptimB, OptimC, and OptimS compatible
883 with the Unitherm database, for deriving the thermodynamic properties of aqueous
884 species from solubility, potentiometry and spectroscopy measurements. Applied
885 Geochemistry 55, 17-27.

886 Sprik, M., Hutter, J. and Parrinello, M. (1996) Ab initio molecular dynamics simulation of
887 liquid water: Comparison of three gradient-corrected density functionals. The Journal of
888 chemical physics 105, 1142-1152.

889 Sprik, M. and Ciccotti, G. (1998) Free energy from constrained molecular dynamics. The
890 Journal of Chemical Physics 109, 7737.

891 Sprik, M. (2000) Computation of the pK of liquid water using coordination constraints.
892 Chemical Physics 258, 139-150.

893 Stefanski, J. and Jahn, S.: Yttrium speciation in subduction zone fluids from ab
894 initio molecular dynamics simulations, Solid Earth Discuss.,
895 https://doi.org/10.5194/se-2019-195, in review, 2020.

896 Tagirov, B.R., Zotov, A.V. and Akinfiev, N.N. (1997) Experimental study of dissociation of
897 HCl from 350 to 500°C and from 500 to 2500 bars: Thermodynamic properties of
898 HCl°(aq). Geochimica et Cosmochimica Acta 61, 4267-4280.

899 Testemale, D., Argoud, R., Geaymond, O. and Hazemann, J.-L. (2005) High pressure/high
900 temperature cell for x-ray absorption and scattering techniques. Review of Scientific
901 Instruments 76, 043905.

902 Testemale, D., Brugger, J., Liu, W., Etschmann, B. and Hazemann, J.-L. (2009) In-situ X-ray
903 absorption study of Iron(II) speciation in brines up to supercritical conditions. Chemical
904 Geology 264, 295-310.

905 Tian, Y., Etschmann, B., Mei, Y., Grundler, P.V., Testemale, D., Hazemann, J.-L., Elliott, P.,
906 Ngothai, Y. and Brugger, J. (2014) Speciation and thermodynamic properties of
907 manganese(II) chloride complexes in hydrothermal fluids: In situ XAS study.
908 Geochimica et Cosmochimica Acta 129, 77-95.

Tu, Y.-J., Lin, Z., Allen, M.J. and Cisneros, G.A. (2018) Molecular dynamics investigation of water-exchange reactions on lanthanide ions in water/1-ethyl-3-methylimidazolium trifluoromethylsufate ([EMIm][OTf]). The Journal of Chemical Physics 148, 024503.

Vala Ragnarsdottir, K., Oelkers, E.H., Sherman, D.M. and Collins, C.R. (1998) Aqueous speciation of yttrium at temperatures from 25 to 340°C at Psat: an in situ EXAFS study. Chemical Geology 151, 29-39.

Weng, Z., Jowitt, S.M., Mudd, G.M. and Haque, N. (2015) A Detailed Assessment of Global Rare Earth Element Resources: Opportunities and Challenges. Economic Geology 110, 1925-1952.

Williams-Jones, A.E., Migdisov, A.A. and Samson, I.M. (2012) Hydrothermal Mobilisation of the Rare Earth Elements - a Tale of "Ceria" and "Yttria". Elements 8, 355-360.

Wood, S.A. The aqueous geochemistry of the rare-earth elements and yttrium. 28.

Xing, Y., Etschmann, B., Liu, W., Mei, Y., Shvarov, Y., Testemale, D., Tomkins, A. and Brugger, J. (2019) The role of fluorine in hydrothermal mobilization and transportation of Fe, U and REE and the formation of IOCG deposits. Chemical Geology 504, 158-176.

Zachariasen, W. (1949) Crystal chemical studies of the 5f-series of elements. XII. New compounds representing known structure types. Acta Crystallographica 2, 388-390.

Table 1 Structure of aqueous Y(III) at room temperature (~25 ˚C) and hydrothermal conditions in literature.

	Methods	conditions	hydration	Y-O distance (Å)	reference	note
Experimental studies	XRD	1.094 m $Y(ClO_4)_3$	8.0 ± 0.3	2.365	Johansson and Wakita, 1985	
	AXS	0.5 M YCl_3	8.1 ± 0.3	2.51 ± 0.02	Matsubara et al., 1990	
		1 M YCl_3	8.2 ± 0.5	2.46 ± 0.02		
	EXAFS	0.5 M YCl_3	7.5	2.33	Marques et al., 1992	No Y-Cl bonds were found in either Raman and EXAFS
		1.0 M YCl_3	8.5	2.33		
		1.2 M YCl_3	7.5	2.34		
	EXAFS	(a) 0.1 M YCl_3	9.1	2.36	Ragnarsdottir et al., 1998	No Y-Cl bonding and hydration decreases by 0.6, 2.6 and 1.8 with temperature increasing up to 340 ˚C for (a) and 250 ˚C for (b) and (c)
		(b) 0.1 M YCl_3 + 0.23M HCl + 1M NaCl	10.2	2.36		
		(c) 0.1 M YCl_3 + 0.23M HCl + 2M NaCl;	10.3	2.37		
	EXAFS&LXAS	1.71 M $Y(ClO_4)_3$ in $HClO_4$	8	2.368 ± 0.003	Lindqvist-Reis et al., 2000	
	EXAFS	0.005 ~ 2 m YBr_3	8	2.353 ± 0.001	Diaz-Moreno et al., 2000	
	EXAFS	0.1 M YCl_3 + 0.25 M HCl/14 M LiCl	9.7/9.6		Allen et al., 2000	
	EXAFS &EPSR	1 m YCl_3	7.5 ± 0.5	2.33	Bowron and Diaz-Moreno, 2007	0.8 ± 0.2 Y-Cl
	RAMAN/ DFT	3.2 M YCl_3 and 2.03 M YCl_3 + (0, 1, 4M HCl)	8-n	2.366	Rudolph and Irmer, 2015	Square antiprism, with n Y-Cl bonds (n = 1,2); n=0 when Cl^- concentration < 0.2 m
Theoretical studies	DFT	1 m YCl_3	8	2.38	Ikeda et al., 2005a, b	Square antiprism structure
	AIMD	1 Y^{3+} in 63 waters' box	8		Liu et al., 2012	

Table 2. Simulation details of *ab initio* MD.

Box No.	Solution composition	Job No.	T (°C)	P (bar)	Box size ($Å^3$)	Density (g/cm^3)
1	55 H_2O, Y^{3+} , $3Cl^-$ (3 m Cl^-)	1a(1,2)	25	1	12.048	1.127
		1b	200	800	12.366	1.042
		1c	350	800	12.999	0.897
		1d	500	800	14.228	0.684
		1e	500	1000	13.940	0.727
2	55 H_2O, Y^{3+} , 4 Cl^- , 1 Na^+ (4 m Cl^-)	2a	200	800	12.443	1.073
		2b	350	800	13.032	0.934
		2c	500	1000	14.122	0.734
3	55 H_2O, Y^{3+} , 5 Cl^-, 2 Na^+ (5 m Cl^-)	3a	200	800	12.526	1.101
		3b	350	800	13.085	0.966
		3c	500	1000	13.865	0.812
4	111 H_2O, Y^{3+} , 5 Cl^-, 1 Na^+, H^+ (2.5 m Cl^-)	4a	200	800	15.577	1.006
		4b	350	800	16.412	0.860
		4c	450	800	17.368	0.726

Table 3. XAS solution compositions.

Sample composition	Serial Number	condition
0.01 m YCl_3 + 0.75 m HCl	Sol 6	30 ˚C – 400 ˚C, 800 bar
0.01 m YCl_3 + 10 m LiCl + 0.5 m HCl	Sol 5	30 ˚C – 450 ˚C, 800 bar
0.01 m YCl_3 + 2 m NaCl + 0.5 m HCl	Sol 7	30 ˚C – 350 ˚C, 800 bar
0.01 m YCl_3 + 1 drop HCl	Sol 3	30 ˚C – 400 ˚C, 800 bar
1 m YCl_3	Sol 12	30 ˚C – 450 ˚C, 800 bar

Table 4. Simulation results by *ab initio* MD, error of coordination was measured from radial distribution function at distance range of 2.75 Å - 3.25 Å for Y-O and 2.9 Å – 3.2 Å for Y-Cl; Debye-Waller can only be measured when there is no ligand exchange in the simulation.

No	T (°C), P (bar)	Time (ps)	Initial configuration	Stable species	Y-Cl			Y-O			CN_{tot}
					N	r(Å)	σ^2 (Å^2)	N	r(Å)	σ^2 (Å^2)	
1a(1)	25, 1	25.37	$[Y(H_2O)_8]^{3+}$	$[Y(OH_2)_8]^{3+}$				8	2.42	0.0106	8
1a(2)	25, 1	23.02	$[Y(H_2O)_7Cl]^{2+}$	$[Y(OH_2)_8]^{3+}$				8	2.42	0.0107	8
1b	200, 800	30.17	$[Y(H_2O)_6Cl_2]^{+}$	$[Y(H_2O)_{5.5}Cl_{1.8}]^{1.2+}$	1.7(0.1)	2.65		5.2(0.1)	2.36		7
1c	350, 800	23.87	$[Y(H_2O)_7Cl_2]^{+}$	$[Y(H_2O)_{4.5}Cl_2]^{+}$	2(0.1)	2.62	0.0172	4.5(0.1)	2.36		6.5
1d	500, 800	22.43	$[Y(H_2O)_5Cl_3]^{0}$	$[Y(OH_2)_3Cl_3]^{0}$	3(0.2)	2.55	0.0155	3(0.2)	2.44		6
1e	500, 1000	26.94	$[Y(H_2O)_5Cl_3]^{0}$	$[Y(OH_2)_3Cl_3]^{0}$	3	2.56	0.0200	3	2.44		6
2a	200, 800	20.30	$[Y(H_2O)_7Cl_2]^{2+}$	$[Y(H_2O)_{5.3}Cl_{1.8}]^{1.2+}$	1.8(0.1)	2.6		5.2(0.1)	2.35		7.1
2b	350, 800	19.21	$[Y(H_2O)_7Cl_2]^{+}$	$[Y(H_2O)_5Cl_2]^{+}$	1.9(0.1)	2.66	0.0236	4.9(0.2)	2.38		7
2c	500, 1000	16.23	$[Y(H_2O)_6Cl_2]^{+}$	$[Y(H_2O)_{4.2}Cl_2]^{+}$	2(0.1)	2.56		4.1(0.2)	2.33		6.2
3a	200, 800	16.06	$[Y(H_2O)_7Cl]^{2+}$	$[Y(OH_2)_5Cl_2]^{+}$	2(0.1)	2.67	0.0168	5(0.1)	2.38		7
3b	350, 800	17.52	$[Y(OH_2)_4Cl_3]^{0}$	$[Y(OH_2)_{3.9}Cl_{2.3}]^{2+}$	2.3(0.1)	2.61		3.9(0.1)	2.35		6.2
3c	500, 1000	17.01	$[Y(H_2O)_3Cl_3]^{0}$	$[Y(OH_2)_2Cl_4]^{-}$	4(0.1)	2.59	0.0194	1.7(0.3)	2.45		5.7
4a	200, 800	22.35	$[Y(H_2O)_8Cl]^{2+}$	$[Y(H_2O)_6Cl]^{2+}$	1	2.63	0.0116	6(0.1)	2.34	0.0155	7
4b	350, 800	16.92	$[Y(OH_2)_5Cl_3]^{0}$	$[Y(OH_2)_{3.7}Cl_2]^{+}$	2	2.63	0.0165	4.1(0.1)	2.36		6.1
4c	450, 800	16.91	$[Y(OH_2)_5Cl_3]^{0}$	$[Y(OH_2)_3Cl_3]^{0}$	3	2.56	0.0191	3.1(0.2)	2.37		6.1

Table 5. EXAFS results.

T (˚C)	nO	rO	nCl	rCl	n_{tot} (first shell)	nY	rY	ss	k-range	R-range
Sol 6			E_0 = 2.2(4)	χ^2_{red} = 661	r-factor = 0.045					
30	8.0 (fix)*	2.369(7)			8	1 (fix)	4.78 (fix)	0.0041(8)	2<k<11	1.1<R<4.5
200	7.0(4)	2.391(8)	(1)		7	1 (fix)	4.78 (fix)	1.4*ssO1	2<k<11	1.1<R<4.5
300	6.4(1)	2.39(1)	0.6(5)	2.60 (fix)	7	1 (fix)	4.78 (fix)	1.6*ssO1	2<k<11	1.2<R<4.5
350	5.2(4)	2.36(1)	1.8(4)	2.68(2)	7	1 (fix)	3.94 (fix)	1.7*ssO1	2<k<10	1.2<R<4.5
400	4.4(4)	2.34(1)	2.6(4)	2.64(1)	7	1 (fix)	3.94 (fix)	1.8*ssO1	2<k<10	1.2<R<4.5
Sol 5			E_0 = 3.3(4)	χ^2_{red} = 523	r-factor = 0.037					
30	7.6(4)	2.388(7)			7.6	1 (fix)	4.74 (fix)	0.0023(3)	2<k<11	1.15<R<4.5
200	6.2(4)	2.398(8)	1.0 (fix)	2.66 (fix)	7.2	1 (fix)	4.74 (fix)	1.4*ssO1	2<k<9	1.15<R<4.5
300	4.0(2)	2.356(8)	2.0(1)	2.68(1)	6	1 (fix)	3.99 (fix)	1.6*ssO1	2<k<10	1.15<R<4.5
350	3.4(1)	2.331(1)	2.6(1)	2.652(9)	6	1 (fix)	3.99 (fix)	1.7*ssO1	2<k<10	1.15<R<4.5
400	3.0(3)	2.338(1)	3.0(1)	2.657(8)	6	1 (fix)	3.99 (fix)	1.8*ssO1	2<k<10	1.15<R<4.5
450	3.0 (fix)	2.326(1)	3.0 (fix)**	2.649(8)	6	1 (fix)	3.99 (fix)	1.9*ssO1	2<k<10	1.15<R<4.5
Sol 7			E_0 = 2.2(4)	χ^2_{red} = 632	r-factor = 0.043					
30	8.0(5)	2.362(8)			8	1 (fix)	4.78 (fix)	0.0041(6)	2<k<11	1.0<R<4.5
200	7.3(4)	2.389(8)	(1)		7.3	1 (fix)	4.78 (fix)	1.4*ssO1	2<k<11	1.0<R<4.5
300	5.8(4)	2.38(1)	1.5(4)	2.70(2)	7.3	1 (fix)	3.99 (fix)	1.6*ssO1	2<k<11	1.0<R<4.5
350	5.1(3)	2.36(1)	2.1(3)	2.67(1)	7.2	1 (fix)	3.99 (fix)	1.7*ssO1	2<k<11	1.0<R<4.5
Sol 3			E_0 = 1.8(4)	χ^2_{red} = 673	r-factor = 0.039					
30	8.0(1)	2.378(8)			8	1 (fix)	4.74 (fix)	0.0050(4)	2<k<11.5	1<R<4.5
200	7.8(3)	2.384(7)	(1)		7.8	1 (fix)	4.74 (fix)	1.4*ssO1	2<k<11	1<R<4.5
300	6.9(3)	2.38(1)	0.9(3)	2.69(6)	7.8	1 (fix)	3.99 (fix)	1.6*ssO1	2<k<11	1<R<4.5
350	6.4(4)	2.37(1)	1.3(4)	2.68(3)	7.7	1 (fix)	3.99 (fix)	1.7*ssO1	2<k<10	1<R<4.5
400	5.7(6)	2.34(1)	2.0(6)	2.64(3)	7.7	1 (fix)	3.99 (fix)	1.8*ssO1	2<k<9	1<R<4.5
Sol 12			E_0 = 0.3(5)	χ^2_{red} = 7725	r-factor = 0.031					
30	8.0(1)	2.374(6)			8	1 (fix)	4.74 (fix)	0.0042(4)	2<k<12	1.1<R<4.0
200	7.9(5)	2.364(7)	0.6(4)	2.60 (fix)	8.5	1 (fix)	4.74 (fix)	1.4*ssO1	2<k<12	1.1<R<4.0
300	6.2(4)	2.36(1)	1.6(4)	2.69(2)	7.8	1 (fix)	3.99 (fix)	1.6*ssO1	2<k<10	1.1<R<4.0

350	5.7(5)	2.36(1)	2.1(4)	2.67(2)	7.8	1 (fix)	3.99 (fix)	1.7*ssO1	2<k<10	1.1<R<4.0
400	5.2(5)	2.35(1)	2.6(5)	2.65(2)	7.8	1 (fix)	3.99 (fix)	1.8*ssO1	2<k<10	1.1<R<4.0
450	4.2(6)	2.35(2)	3.1(1)	2.64(2)	7.3	1 (fix)	3.99 (fix)	1.9*ssO1	2<k<10	1.1<R<4.0

NOTE: applied constraints, i.e. nCl @ $T_i \leq$nCl @ T_{i+1}, and n_{tot} @ $T_i \geq n_{tot}$ @ T_i.

*fix based on everyone else's determination of n=8 at ambient conditions, use this to determine S_0^2.

**Data at 450˚C is noisier than at 400˚C; equally good fits are obtained up to $n_{Cl} = 3.3$.

Table 6. Gibbs free energy of reactions and stepwise stability constants of Y(III)-Cl association reactions, calculated from box 1 and box 3. $\Delta_r G$, Gibbs free energy for the reaction; $\Delta_r G^{\Theta,c}$, Gibbs free energy at infinite dilution; $\Delta_r G^{\Theta}$, Gibbs free energy with concentration and activity correction.

Reaction in box 1	T(°C), P(bar)	$\Delta_r \boldsymbol{G}$ (kJ/mol)	$\Delta_r G^{\Theta,c}$ **(kJ/mol)**	$\Delta_r G^{\Theta}$ **(kJ/mol)**	**logK^{Θ}**
$Y^{3+} + Cl^- = YCl^{2+}$	200, 800	-3.92 ± 8.85	3.60	-8.27	0.91 ± 0.98
	350, 800	-24.35 ± 10.42	-14.46	-55.96	4.69 ± 0.87
	500, 1000	-50.34 ± 11.60	-38.06	-146.44	9.89 ± 0.78
$YCl^{2+} + Cl^- = YCl_2^+$	200, 800	1.84 ± 9.21	7.30	-1.53	0.17 ± 1.01
	350, 800	-26.48 ± 10.11	-19.30	-45.33	3.80 ± 0.87
	500, 1000	-37.31 ± 11.37	-28.40	-93.27	6.30 ± 0.77
Reaction in box 3					
$Y^{3+} + Cl^- = YCl^{2+}$	200, 800	-12.05 ± 8.01	-2.21	-9.95	1.01 ± 0.89
	350, 800	-28.22 ± 9.48	-15.26	-58.19	4.88 ± 0.79
	500, 1000	-36.07 ± 10.06	-19.98	-142.58	9.63 ±0.68
$YCl^{2+} + Cl^- = YCl_2^+$	200, 800	-2.12 ± 8.74	6.73	0.64	-0.07 ± 0.96
	350, 800	-26.23 ± 10.72	-14.58	-42.32	3.55 ± 0.90
	500, 1000	-30.62 ± 9.86	-16.16	-92.95	6.28 ± 0.67
$YCl_2^+ + Cl^- = YCl_3(aq)$	200, 800	2.70 ± 9.69	10.21	8.12	-0.90 ± 1.07
	350, 800	-12.19± 9.36	-2.30	-16.15	1.35 ± 0.78
	500, 1000	-33.39 ± 9.97	-21.12	-61.74	4.17 ± 0.67
$YCl_3(aq) + Cl^- = YCl_4^-$	200, 800	1.29 ± 8.46	6.75	6.75	-0.74 ± 0.93
	350, 800	-5.76 ± 9.15	1.42	1.42	-0.12 ± 0.77
	500, 1000	-17.84 ± 10.63	-8.93	-8.93	0.60 ± 0.72

Table 7. Cumulative formation constant of Y(III)-Cl complexes.

Reaction	**T(°C), P(bar)**	**logβ^{θ}**	***error***
Y^{3+} + Cl^- = YCl^{2+}	200, 800	0.96	0.66
	350, 800	4.79	0.59
	500, 1000	9.76	0.50
Y^{3+} + 2 Cl^- = YCl_2^+	200, 800	1.01	0.95
	350, 800	8.47	0.86
	500, 1000	16.05	0.71
Y^{3+} + 3 Cl^- = YCl_3(aq)	200, 800	0.11	1.43
	350, 800	9.82	1.16
	500, 1000	20.22	0.98
YCl_3(aq) + Cl^- = YCl_4^-	200, 800	-0.63	1.71
	350, 800	9.70	1.39
	500, 1000	20.82	1.22

Table 8. Modified Ryzhenko–Bryzgalin (MRB) (Ryzhenko et al., 1985; Shvarov and Bastrakov, 1999) equation of state parameters for the Y(III)-Cl complexes obtained via fitting of $\log K^{\Theta}$ values from MD simulations. *The B parameters were set to zero, except for the association reaction of $Y^{3+} + Cl^{-} = YCl^{2+}$, whose $\log\beta^{\Theta}_{(25^{\circ}C,1\ bar)}$? was chosen from Luo & Byrne (2001). [you have K is italics sometimes...]

reaction	$\log\beta^{\Theta}_{(25^{\circ}C,1\ bar)}$	$\mathbf{A_{zz}}$	$\mathbf{B_{zz}}$*
$Y^{3+} + Cl^{-} = YCl^{2+}$	0.65	3.357	-1428
$Y^{3+} + 2\ Cl^{-} = YCl_2^{+}$	-8.314	3.047	-
$Y^{3+} + 3\ Cl^{-} = YCl_3(aq)$	-12.914	3.97	-
$Y^{3+} + 4\ Cl^{-} = YCl_4^{+}$	-14.800	4.176	-

Table 9. the logarithm of formation constant Y(III)-Cl complexes calculated using MRB parameters in Table 8. *, values are used in discussion part.

T (˚ C)	P_{Sat}	800 bar	1000 bar	2000 bar	5000 bar	P_{Sat}	800 bar	1000 bar	2000 bar	5000 bar
	$Y^{3+} + Cl^- = YCl^{2+}$					$Y^{3+} + 2\ Cl^- = YCl_2^+$				
25	0.65	1.04	1.13	1.51	2.26	-8.31	-9.14	-9.33	-10.14	-11.74
50	0.22	0.48	0.54	0.81	1.36	-6.58	-7.34	-7.51	-8.27	-9.86
100	0.02	0.13	0.16	0.27	0.51	-3.38	-4.14	-4.30	-5.03	-6.61
150	0.43	0.43	0.43	0.44	0.45	-0.50	-1.37	-1.55	-2.33	-3.96
200	1.24	1.12	1.09	0.99	0.80	2.21*	1.12	0.90	0.01	-1.76
250	2.37*	2.06	2.00	1.78	1.37	4.96*	3.46	3.18	2.09	0.12
300	3.87*	3.21	3.10	2.71	2.07	8.11	5.78	5.40	4.02	1.76
350	6.21*	4.58	4.39	3.75	2.84	12.90	8.24	7.68	5.87	3.24
400		6.26	5.90	4.89	3.64		11.05	10.15	7.68	4.60
450		8.39	7.69	6.13	4.48		14.48	12.94	9.49	5.86
500		11.14	9.85	7.45	5.33		18.77	16.16	11.32	7.05
	$Y^{3+} + 3\ Cl^- = YCl_3(aq)$					$Y^{3+} + 4\ Cl^- = YCl_4^+$				
25	-12.91	-14.00	-14.24	-15.30	-17.38	-14.80	-15.94	-16.19	-17.31	-19.50
50	-10.49	-11.48	-11.71	-12.69	-14.77	-12.16	-13.20	-13.43	-14.47	-16.66
100	-6.07	-7.06	-7.27	-8.22	-10.28	-7.35	-8.39	-8.62	-9.62	-11.78
150	-2.12	-3.25	-3.49	-4.50	-6.62	-3.09	-4.27	-4.52	-5.59	-7.82
200	1.56	0.14	-0.14	-1.30	-3.60	0.88	-0.61	-0.91	-2.14	-4.55
250	5.27*	3.32	2.95	1.54	-1.03	4.85	2.79	2.41	0.93	-1.78
300	9.49	6.45	5.95	4.16	1.22	9.35	6.15	5.62	3.74	0.65
350	15.82	9.74	9.01	6.65	3.23	16.06	9.67	8.89	6.41	2.81
400		13.47	12.30	9.08	5.07		13.63	12.40	9.01	4.79
450		18.01	16.00	11.50	6.77		18.45	16.33	11.60	6.62
500		23.65	20.25	13.94	8.38		24.41	20.84	14.20	8.35

Figure 1. Snapshots of Y(III)-Cl complexes at different T, P from MD simulations. (a-d) are configurations obtained from simulations of box 1 under condition of 25 ˚C 1 bar; 200 ˚C, 800 bar; 350 ˚C, 800 bar; 500 ˚C, 1000 bar, respectively; (f) is the configuration derived at 500 ˚C and 1000 bar in box 3.

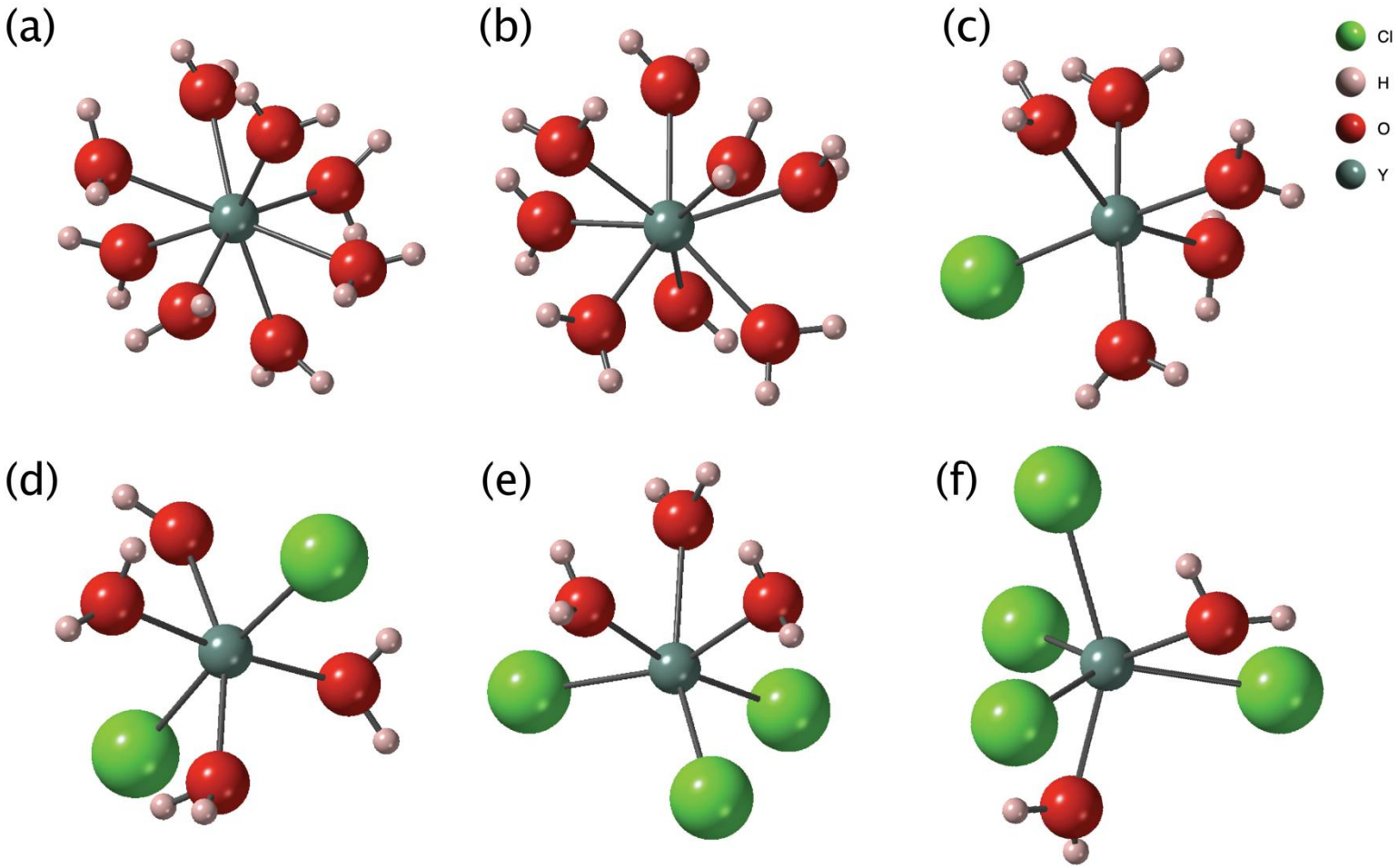

Figure 2, Radial distribution functions (RDF, left axes, solid lines) and their integrals (coordination number, CN, right axes, dash lines) of Y(III)-Cl and Y(III)-O (x-axis) in the four boxes of simulations, (a), (b), box 1; (c),(d), box 2; (e), (f), box 3; (g), (h), box 4.

Box 1

Box 2

Box 3

Box 4

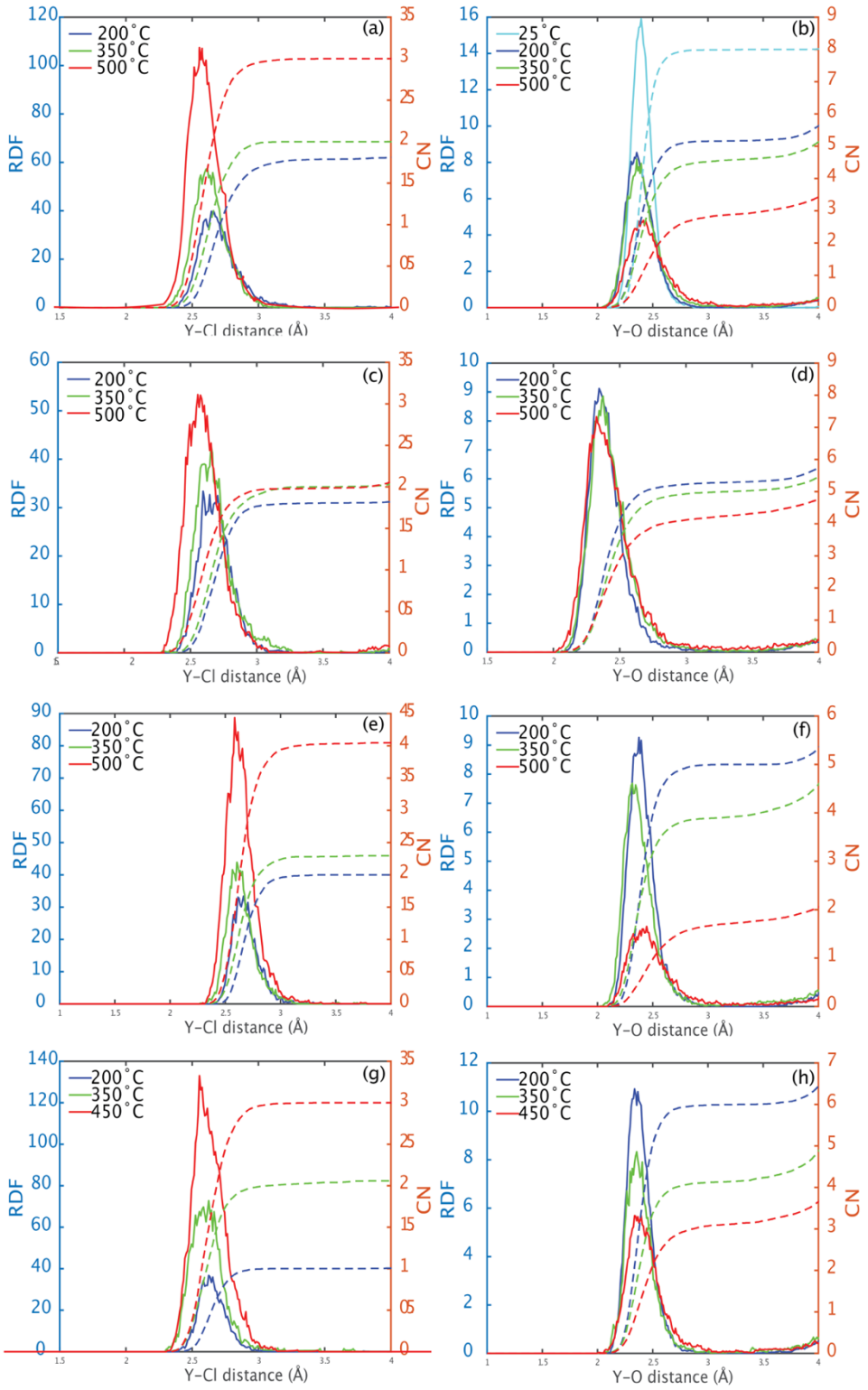

Figure 3. Y(III)-Cl distances over simulation time of (a), job 1a(2) and (b), 1b.

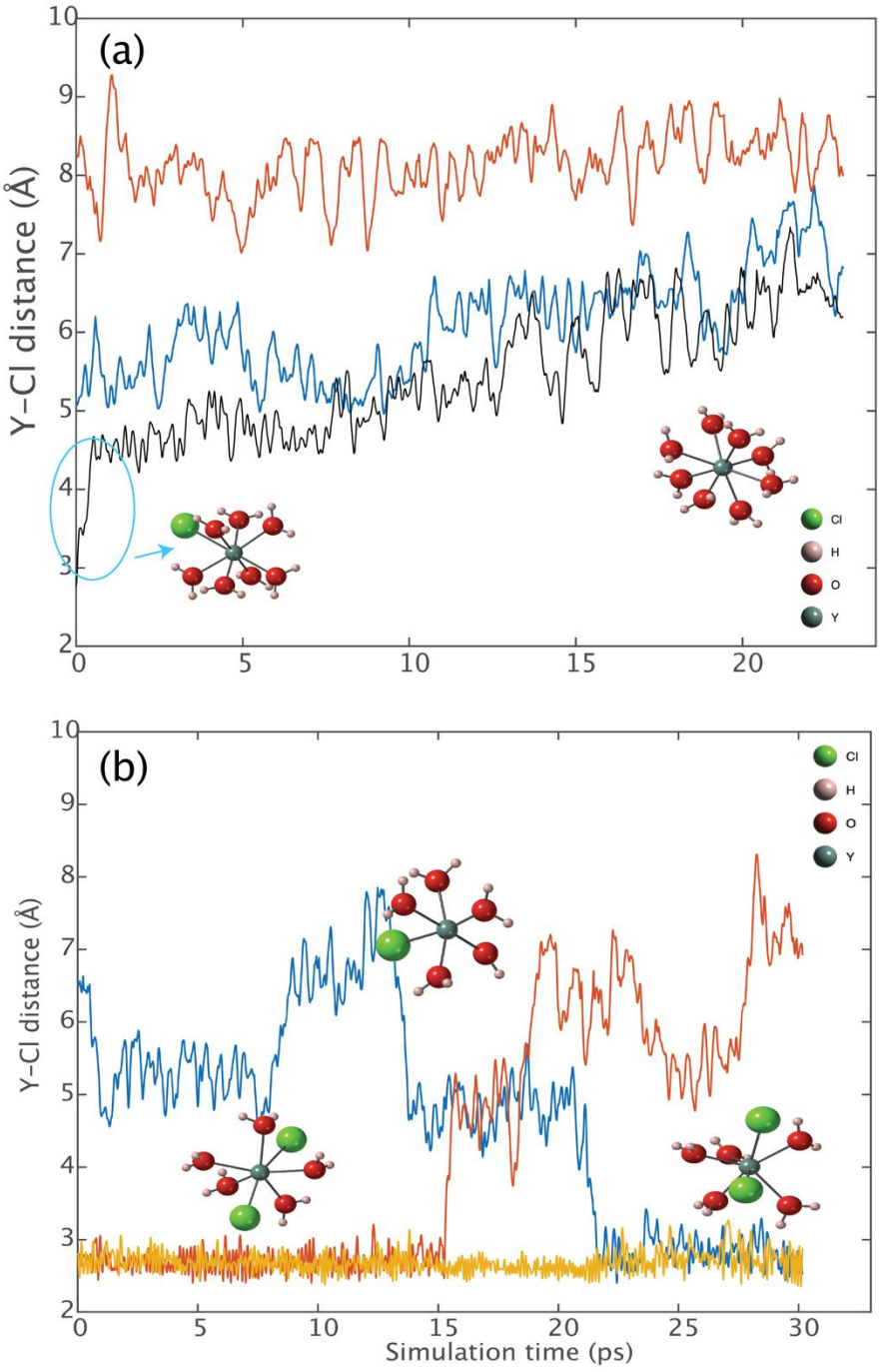

Figure 4. XANES spectra on the solution with highest chlorine concentration (Sol5; 10 m LiCl) as a function of temperature.

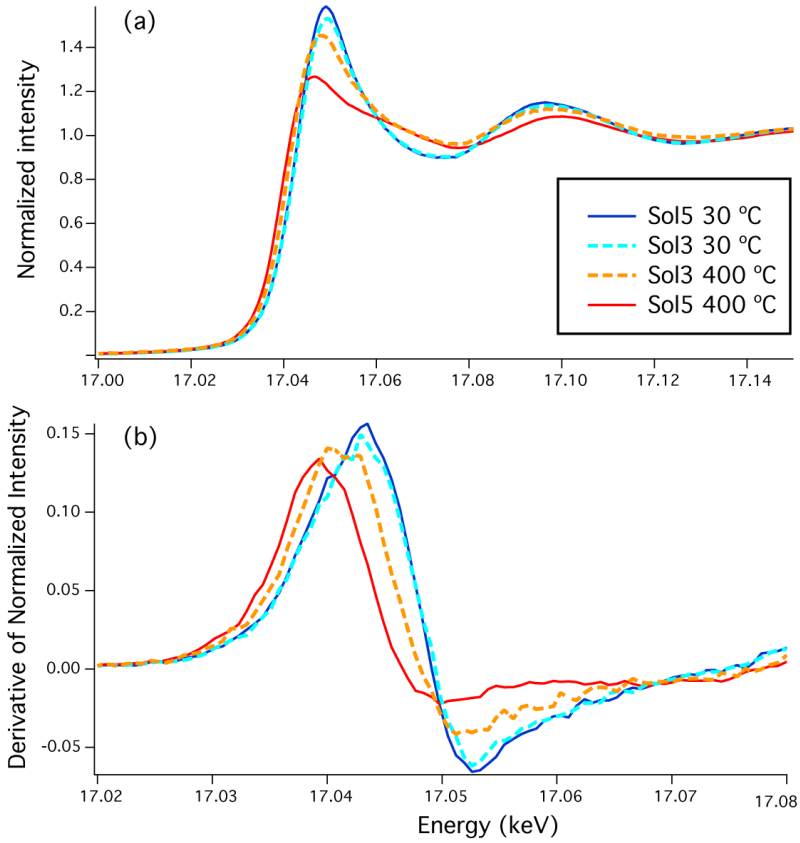

Figure 5. EXAFS data (solid lines) and shell-by-shell fits (dotted lines).

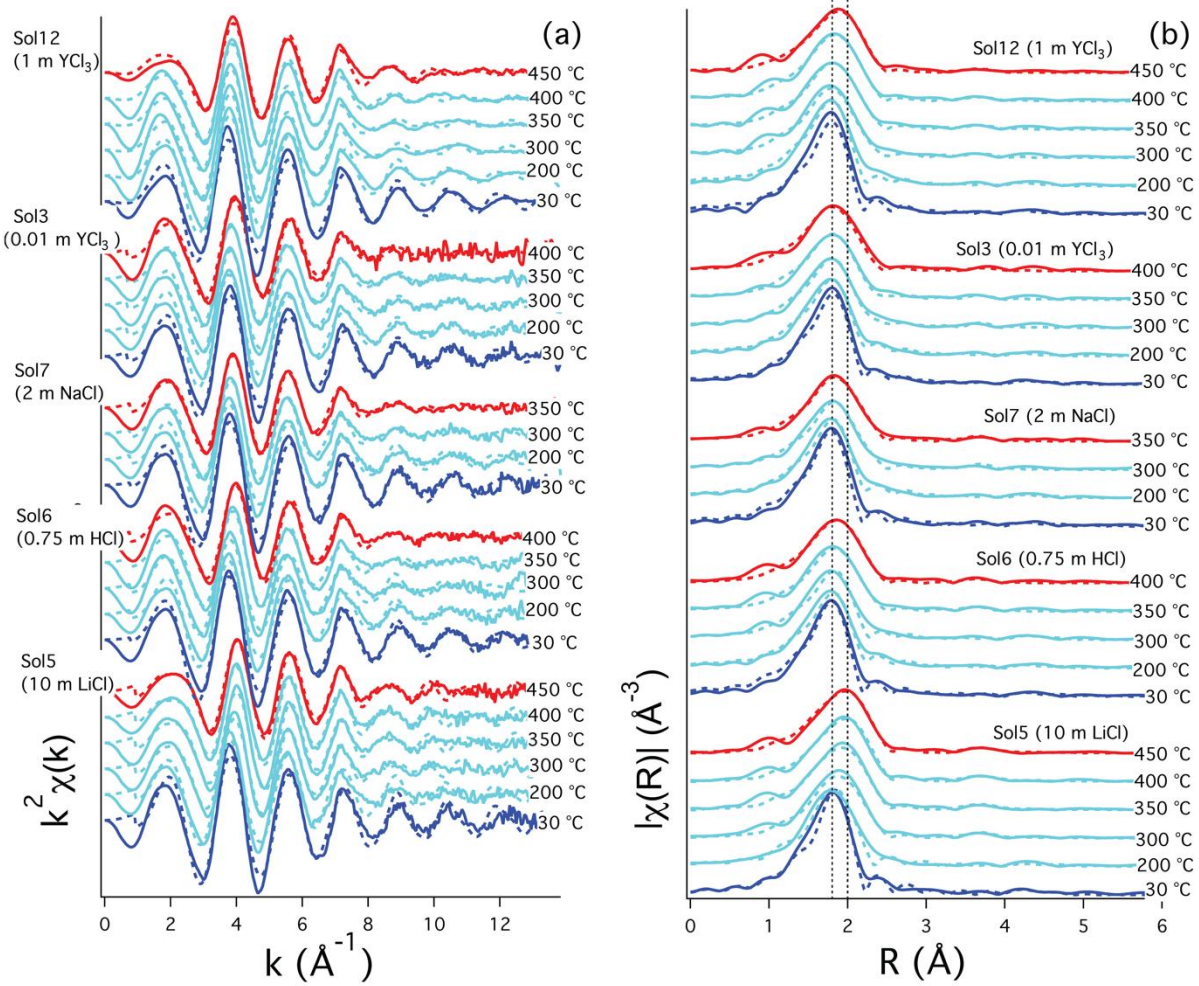

Figure 6. Experimental and calculated XANES spectra: The Yttrium K-edge (17,038 eV) was substracted from the experimental energy to compared with the FDMNES spectra. (a) crystalline Y_2O_3(s); the crystal structure used for FDMNES is from Santos et al. (2005); (b) antiprism [YO_8] moiety with different bond distance (r) and angle between Y-O bond and z axis (angle θ); (c) triangular prismatic [YCl_nO_{6-n}] ($n \leq 3$) moiety with bond distances $r_{Y\text{-}O}$ = 2.37 Å and $r_{Y\text{-}Cl}$ = 2.65 Å, compared to selected Y-O-Cl complexes from the MD simulations; and (d) the average of calculated spectra from MD boxes compared to experimental spectra over a range of conditions.

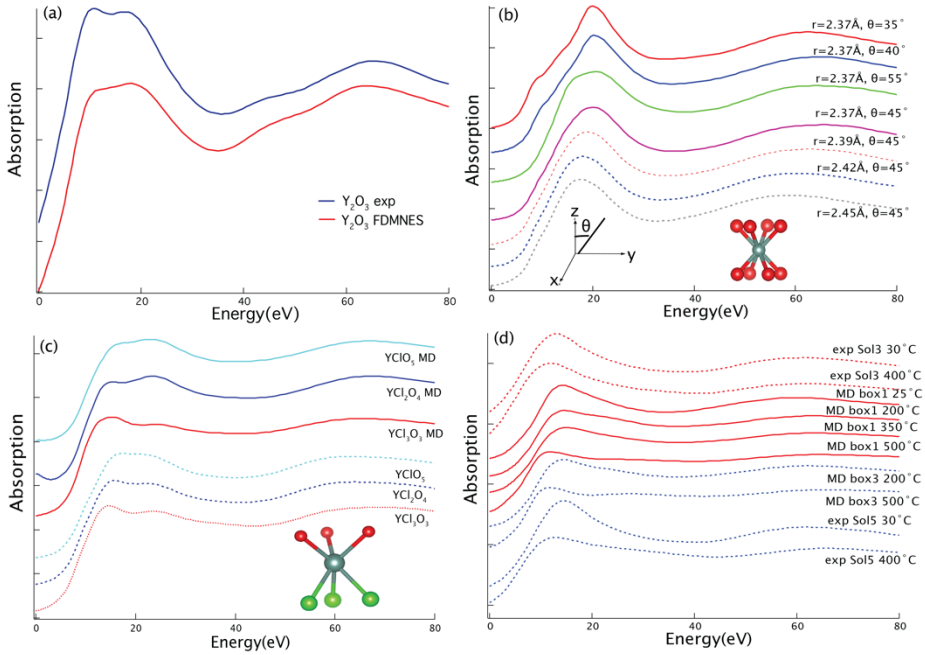

Figure 7. Constraint mean force and free energy surface of dissociation reaction of YCl^{2+} at 200 ˚C, 800 bar.

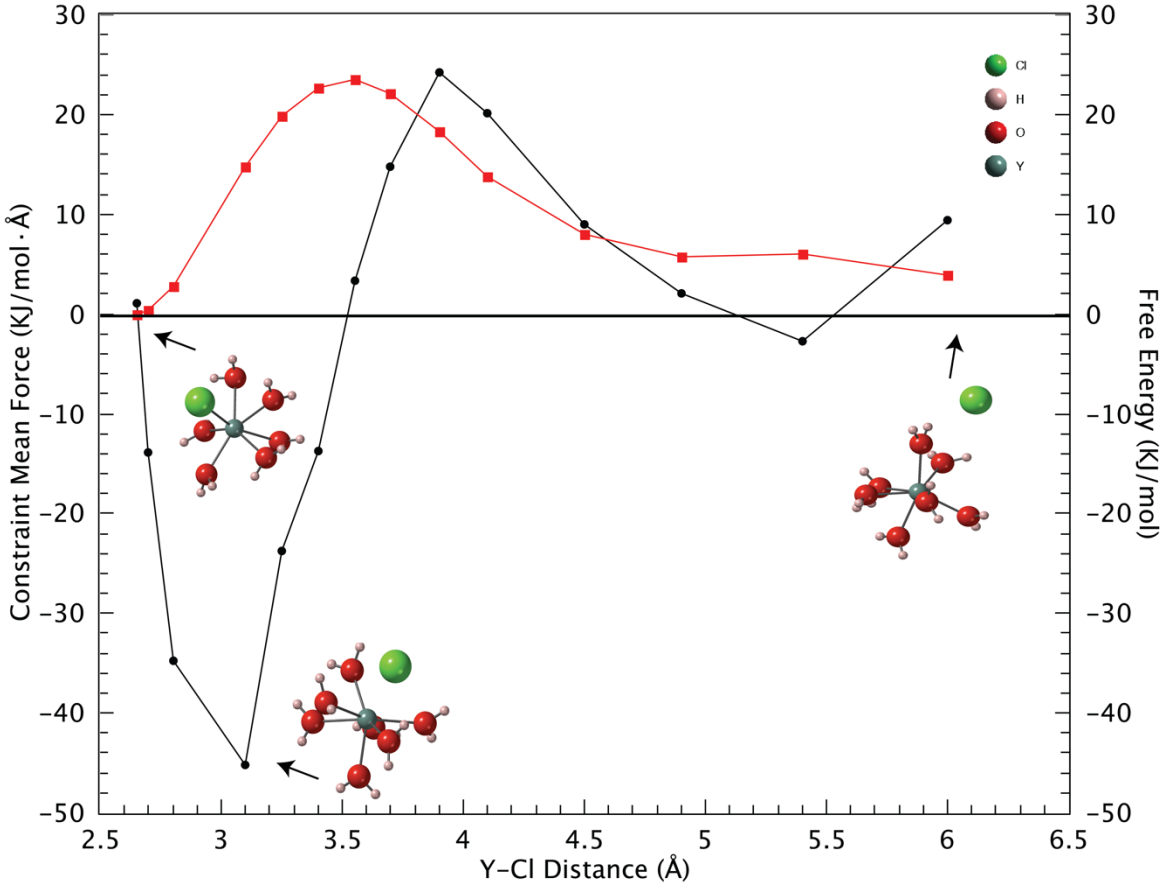

Figure 8. Free energy surface of Y(III)-Cl complexes at 200 ˚C, 800 bar; 350 ˚C, 800 bar; 500 ˚C, 1000 bar from thermodynamic integration calculation in box 1 (a - c) and box 3(d - f).

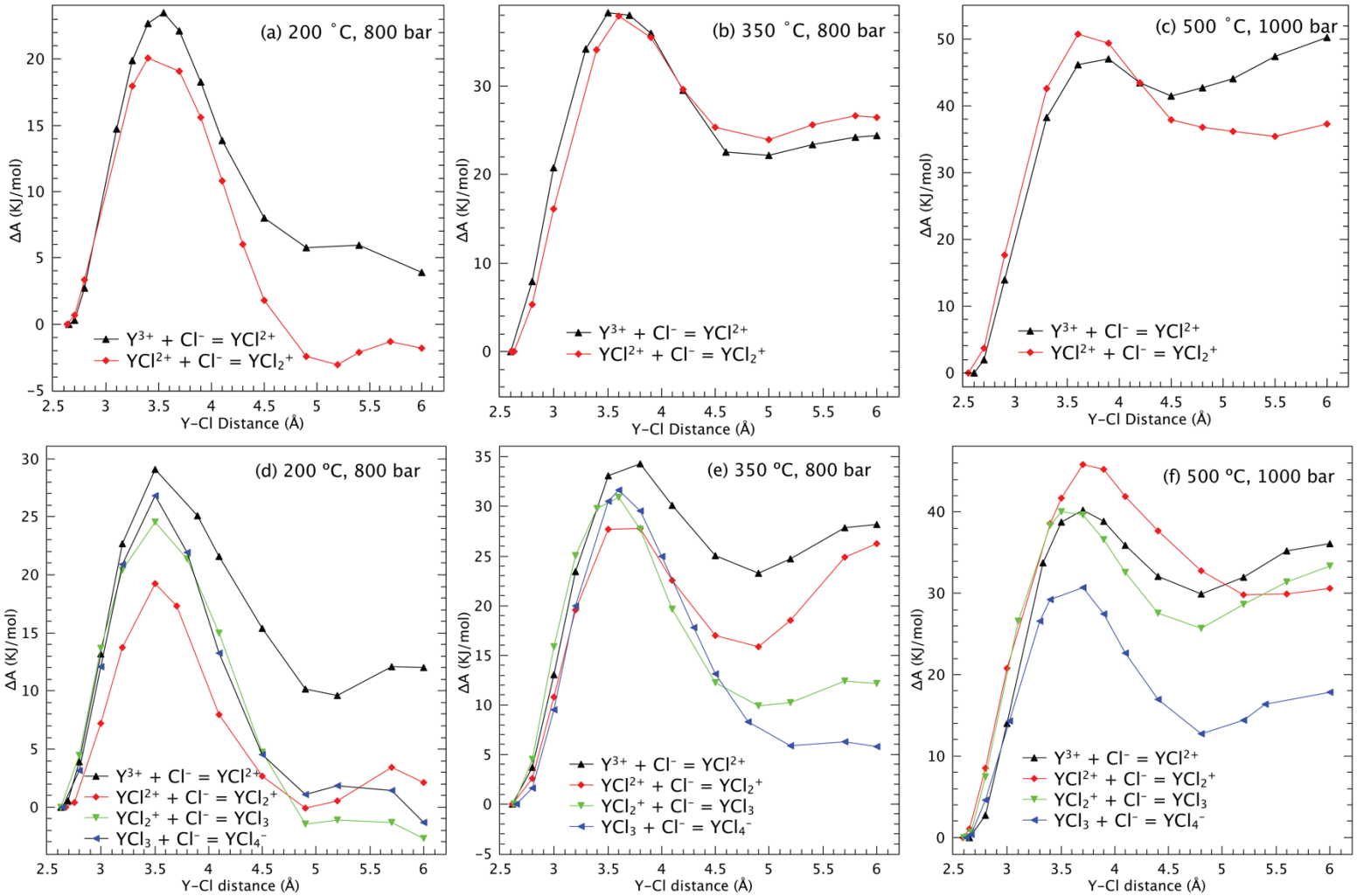

Figure 9. The stepwise logK^{Θ} of association of Y(III)-Cl complexes at 200 ˚C, 800 bar; 350 ˚C, 800 bar; 500 ˚C, 1000 bar and within error bar, and the average value of the two boxes.

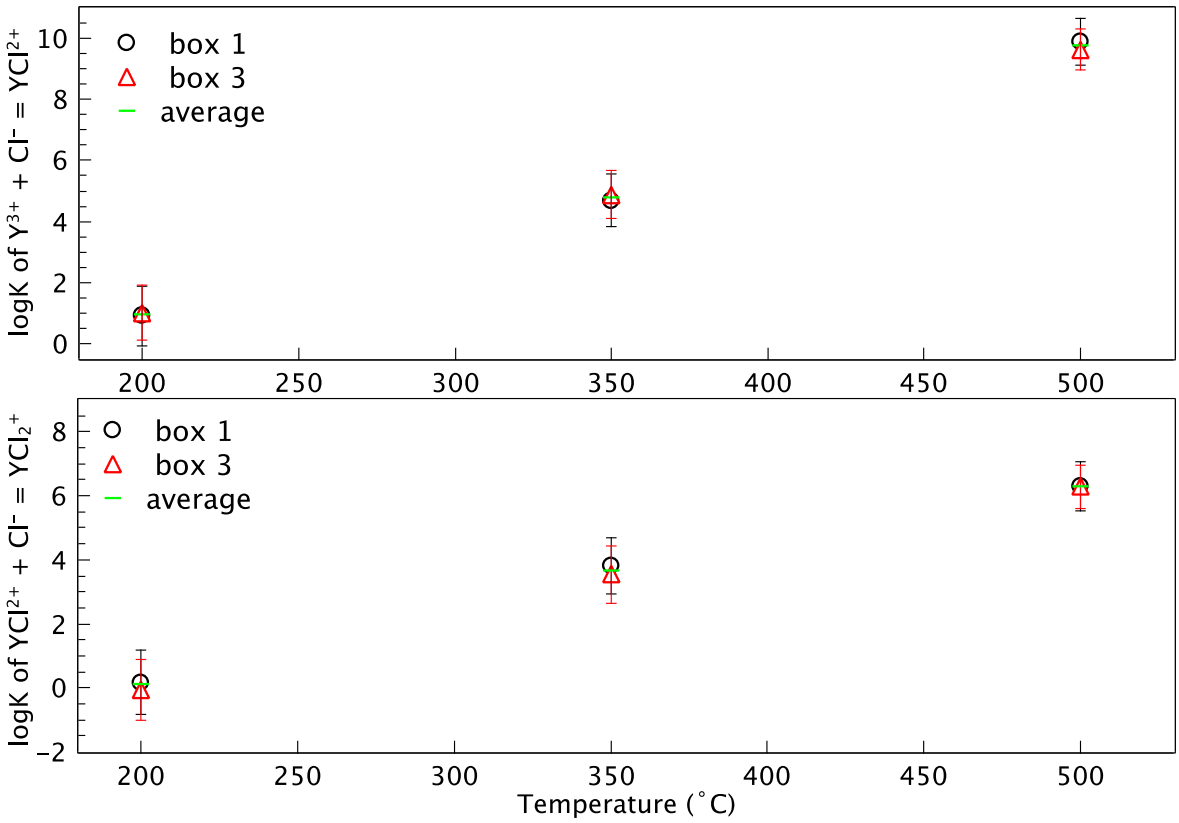

Figure 10. Coordination number (CN) of chloride (triangle), oxygen (H_2O, circle) and total CN of yttrium (square), obtained from MD and XAS.

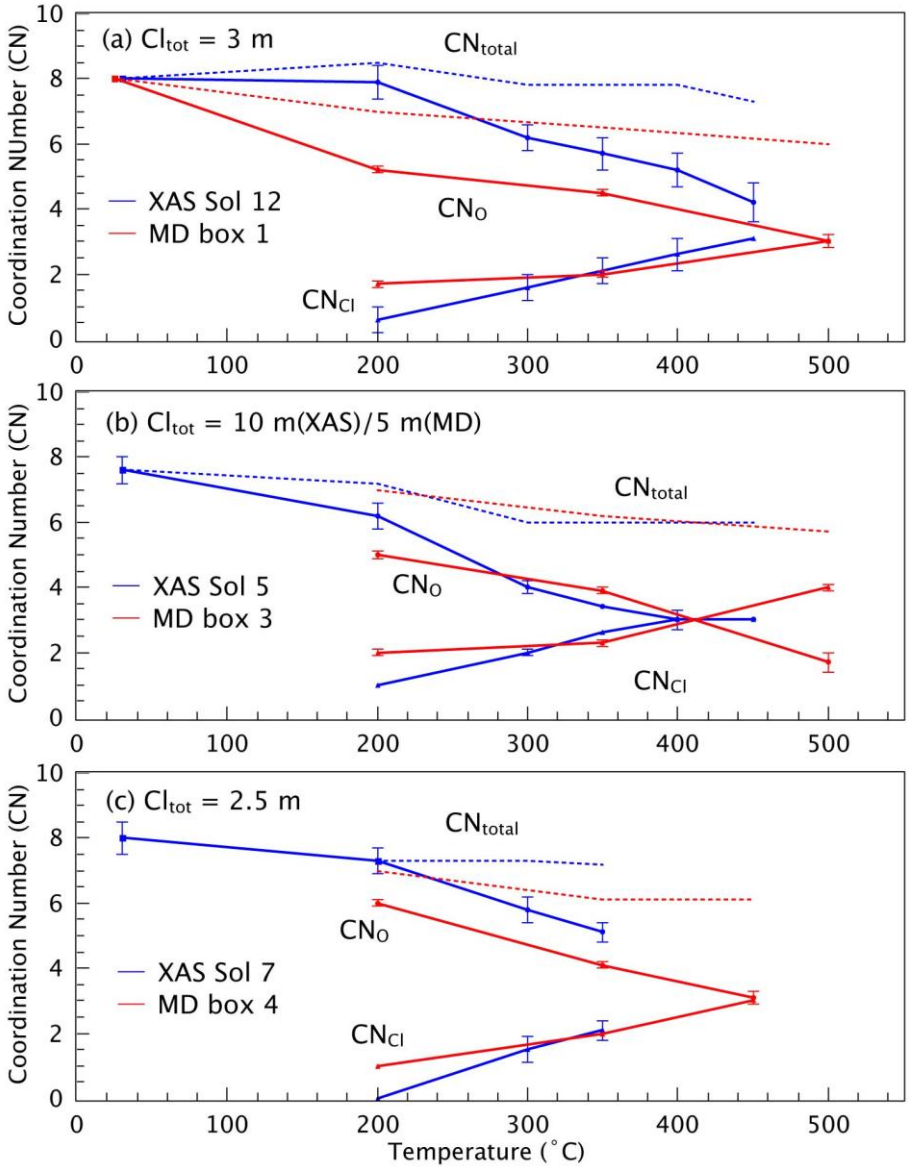

Figure 11. The distribution of Y(III) chloride species at 200 ˚C, 800 bar; 350 ˚C, 800 bar; 500 ˚C, 1000 bar, and pH =3 and 0.3. The solution starts with 0.01 m of Y^{3+} and 0.03 m Cl^-. Dashed lines are average coordination numbers (right axis) from the modelled distribution of species, orange dots are average coordination numbers from XAS Sol 3 at n(Cl^-) = 0.003 m (a); Sol 7 at n(Cl^-) = 2.5 m and (b,c) Sol 5 at n(Cl^-) = 5 m (b,d,f). Errors bars corresponding to ±0.2 Cl^- ions were added for XAS solutions where this number was fixed, based on fits using different fixed numbers.

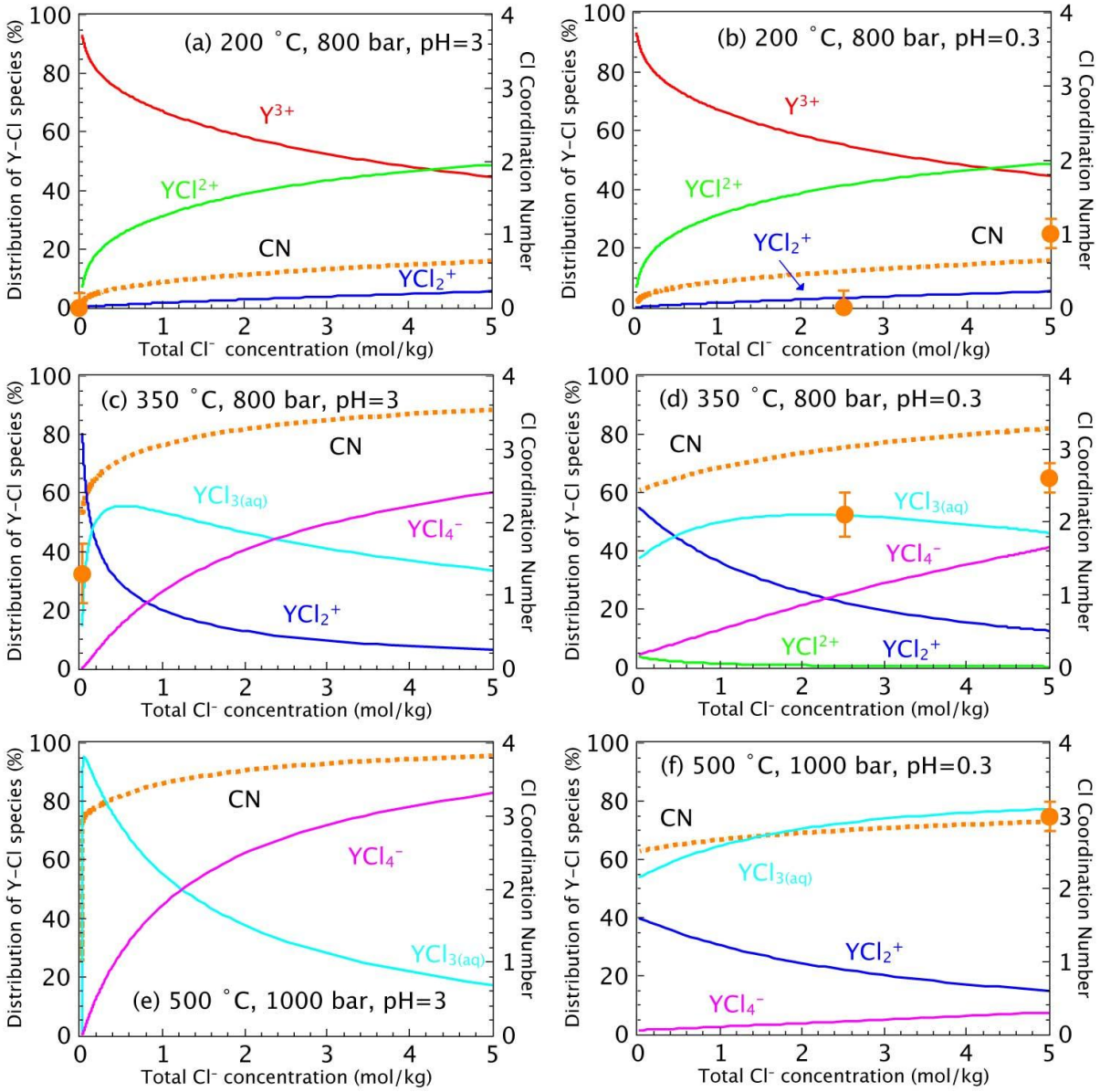

Figure 12. Comparison of the formation constants of $REECl^{2+}$ and $REECl_2^{+}$,●, measured from solubility experiment from Migdisov (2009); ∇, predicted from HKF parameters from Migdisov (2016); ×, predicted from MRB model in this study.

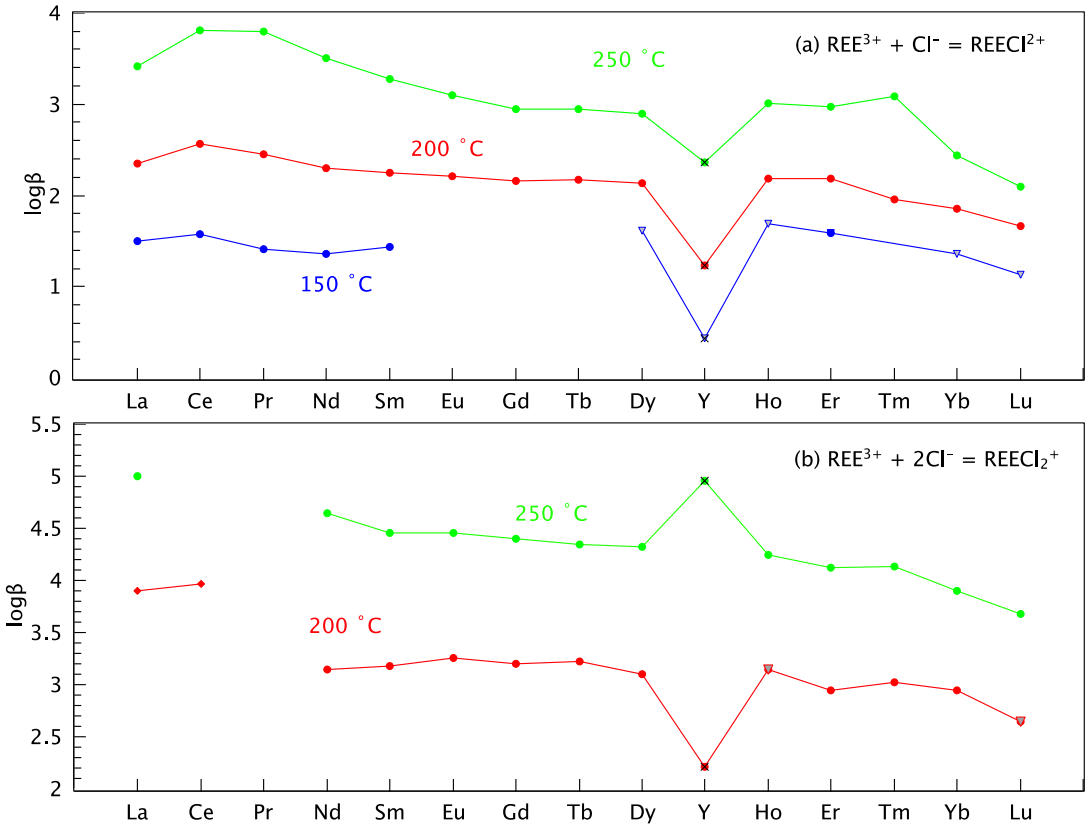

Figure 13. Ho-Cl/Y-Cl species with Cl concentration at 250 ˚C P_{sat}, . The solution starts with 0.001 m Y/Ho and 0.003 m Cl^-, pH=4.